

Geometry, anomaly, topology, and transport in Weyl fermions

Azaz Ahmad, Gautham Varma K., and Gargee Sharma

School of Physical Sciences, Indian Institute of Technology Mandi, Mandi 175005, India.

Weyl fermions are one of the simplest objects that link ideas in geometry and topology to high-energy physics and condensed matter physics. Although the existence of Weyl fermions as elementary particles remains dubious, there is mounting evidence of their existence as quasiparticles in certain condensed matter systems. Such systems are termed Weyl semimetals (WSMs). Needless to say, WSMs have emerged as a fascinating class of materials with unique electronic properties, offering a rich playground for both fundamental research and potential technological applications. This review examines recent advancements in understanding electron transport in Weyl semimetals (WSMs). We begin with a pedagogical introduction to the geometric and topological concepts critical to understanding quantum transport in Weyl fermions. We then explore chiral anomaly (CA), a defining feature of WSMs, and its impact on transport phenomena such as longitudinal magnetoconductance (LMC) and the planar Hall effect (PHE). The Maxwell-Boltzmann transport theory extended beyond the standard relaxation-time approximation is then discussed in the context of Weyl fermions, which is used to evaluate various transport properties. Attention is also given to the effects of strain-induced gauge fields and external magnetic fields in both time-reversal broken and inversion asymmetric inhomogeneous WSMs. The review synthesizes theoretical insights, experimental observations, and numerical simulations to provide a comprehensive understanding of the complex transport behaviors in WSMs, aiming to bridge the gap between theoretical predictions and experimental verification.

CONTENTS

I. INTRODUCTION

I. Introduction	1
A. Overview	1
B. Geometry and quantum physics	2
C. Quantum geometry and Weyl fermions	3
D. Topological Weyl fermions in condensed matter physics	4
E. Chiral anomaly of Weyl fermions	5
II. Electron transport in Weyl fermions	6
A. Maxwell-Boltzmann transport theory of Weyl fermions	6
B. Beyond constant relaxation-time approximation	9
III. Anomalous transport responses	10
A. Longitudinal magnetoconductance	10
1. Single node LMC	10
2. Single node LMC from Landau levels	11
3. Two-node LMC with internode scattering:	13
4. Inclusion of inelastic scattering	14
B. Magnetotransport in inhomogeneous Weyl semimetals	15
C. Planar Hall effect	17
D. Inversion asymmetric WSM	18
IV. Outlook	20
References	21

A. Overview

The role of topology in quantum condensed matter systems has been a subject of extensive study and exploration for the past forty years. The genesis can be traced back to the discovery of the integer and fractional quantum Hall effects in the 1980s [1, 2], which were the first few examples of states of matter topologically distinct from all previously known states. For example, the integer quantum Hall state of matter does not break any symmetries but is characterized by a topological invariant, which leads to a precise quantization of the Hall conductance (ne^2/h) regardless of the microscopic details [3, 4]. The fractional quantum Hall states lead to fractional quantization of Hall conductance $[(p/q)e^2/h]$ arising from an interplay between interactions and topology [5]. The study of the quantum Hall effects and its ramifications led to a new classification paradigm centered on the concept of topological order [6]. Concurrently, ideas establishing the role of geometry in quantum mechanics have flourished as well ever since Berry explored holonomy in adiabatic electronic transport [7]. The study of topology and geometry in condensed matter gained rapid attention in the 2000s following the discovery of graphene and topological insulators [8–11]. Today, the roles of topology, geometry, and the Berry phase in electronic transport in crystals are now firmly established [12–15]. The understanding and manipulation of these concepts have opened up new avenues for research and potential applications in electronic devices and quantum computing.

In a seemingly unrelated context, the history of Weyl and Dirac fermions spans nearly a hundred years. In

1928, Dirac [16] attempted the quantum solution of a relativistic electron and derived the eponymous Dirac equation, which describes an electron of mass m and momentum \mathbf{p} as a four-component spinor dispersing as $\epsilon_{\mathbf{p}} = \sqrt{p^2 c^2 + m^2 c^4}$. When $m = 0$, Dirac's solution can be reformulated as two distinct two-component fermions with opposite chiralities, known as Weyl fermions [17]. Since the past ten years, Weyl fermions (WFs) have surprisingly resurged in condensed matter physics by appearing as quasiparticle excitations in a class of certain (semi)metallic systems, known as Weyl semimetals (WSMs) [18, 19]. It turns out that a WSM phase can appear at the critical point between a topological and a trivial insulator, serving as an intermediate phase in the topological phase transition [20–22]. WSM is itself a stable and topological phase, characterized by gapless Weyl fermionic excitations in the bulk, which are protected by translation symmetry. Furthermore, they exhibit peculiar Fermi arc surface states, which are projections of the gapless points in the Brillouin zone [23–25]. Weyl fermions thus lie at the intersection of topology, geometry, high-energy physics, and condensed matter, making its study highly rewarding from multiple perspectives. Over the past decade, several theoretical predictions and experimental verifications of the WSM phase have been made in systems such as TaAs, NbAs, TaP, NbP, MoTe2, and WTe2 [26–39].

The flow of electrons in WSMs is a problem that has garnered significant attention as well. What makes electron transport fascinating in WSMs is the unique interplay between their geometric and topological properties and high-energy physics phenomena, enabling the emergence of exotic, anomalous, and topological features not found in conventional metallic compounds. The most famous effect in WFs is the so-called chiral anomaly (CA). It originates from high-energy physics [40, 41], where the conservation of left- and right-handed Weyl fermions is violated in the presence of non-orthogonal electric and magnetic fields. This anomaly has reemerged in the study of WSMs and has attracted significant interest in the condensed-matter community [15, 19, 22, 23, 36, 42–63]. In WSMs, which host Weyl fermions as quasiparticle excitations, chiral anomaly is also expected to manifest under external electromagnetic fields. Key transport signatures of this anomaly include positive longitudinal magnetoelectricity (LMC) [45] and the planar Hall effect (PHE) [64]. Intense efforts have been devoted to understanding these anomaly-induced conductivities in WSMs [44–72]. Additionally, non-electronic probes such as optical processes can also indicate the presence of a chiral anomaly [73–79]. Remarkably, strain induces axial vector fields in Weyl semimetals and affects its electronic and thermal transport, adding on to the list of unconventional behavior realized in WSMs [69, 80].

In this work, we present a comprehensive overview of some recent developments in electronic transport studies of WSMs. In Sec. IB, we start by presenting an intuitive picture of geometry, curvature, and topology in the con-

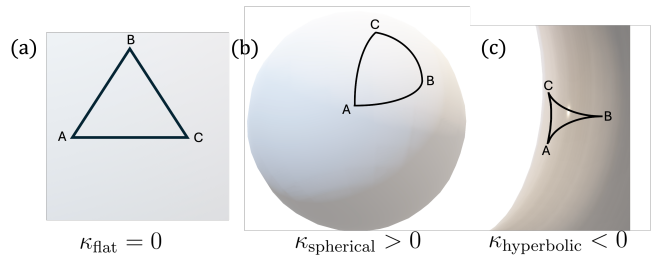


Figure 1. Geometry of different surfaces can be characterized by their curvature κ . The properties of objects existing on surfaces of different curvatures are different. For example, the sum of angles of a triangle drawn equals (a) π for a flat surface, (b) greater than π for a spherical, and (c) less than π for a hyperbolic surface.

text of quantum transport. In Sec. IC and ID, we then connect the seemingly different areas of quantum geometry and WFs, and their relevance in modern condensed matter physics. Sec. IE introduces chiral anomaly in Weyl fermions. Section II presents the Boltzmann electronic transport formalism for Weyl semimetals, while Sec. III presents recent results of longitudinal magnetoelectricity, planar Hall effect, and the effects of strain in inhomogeneous WSMs.

B. Geometry and quantum physics

The geometry of space is fundamental in determining the properties of objects existing in it. The following example makes this more apparent. Consider a triangle in a flat space. Euclidean geometry predicts that the sum of angles of a triangle equals π . If one instead attempts to draw a triangle on a sphere, straight lines in flat space become geodesics, which connect two points by the shortest distance. In this case, the sum of the angles of the triangle is always greater than π , which is a characteristic of spherical geometry. If we repeat the exercise on a surface with hyperbolic geometry, the sum of the angles of a triangle is now less than π (see Fig. 1). One can then define curvature (κ) as the angular excess $\epsilon(\triangle)$ (sum of the angles of a triangle minus π) per unit area $\mathcal{A}(\triangle)$ [81]:

$$\kappa = \frac{\Sigma_{\text{angles}}(\triangle) - \pi}{\text{area}} \equiv \frac{\epsilon(\triangle)}{\mathcal{A}(\triangle)}. \quad (1)$$

The geometry of the three spaces discussed above can then be characterized by their respective curvatures (also see Fig. 1):

$$\begin{aligned} \kappa_{\text{flat}} &= 0 \\ \kappa_{\text{spherical}} &> 0 \\ \kappa_{\text{hyperbolic}} &< 0. \end{aligned}$$

On more general surfaces the curvature may not be constant, and one can instead define a local (or Gaussian)

curvature κ_p at every point p on the surface:

$$\kappa_p = \lim_{\Delta_p \rightarrow p} \frac{\epsilon(\Delta_p)}{\mathcal{A}(\Delta_p)}. \quad (2)$$

For example, the inner surface of a torus has $\kappa < 0$ but the outer surface has $\kappa > 0$.

We can then imagine smoothly stretching a surface such that the lengths and angles of a triangle drawn on the surface are not preserved but no additional cuts or holes are introduced or removed from the surface (see Fig. 2 (a)). Mathematically, such a transformation is termed *homeomorphism*. A famous theorem by Gauss (the Gauss-Bonnet theorem) states that the total curvature of the surface is conserved under homeomorphism [81, 82]:

$$\Sigma_p \kappa(p) \xrightarrow{\text{homeomorphism}} \text{constant}. \quad (3)$$

The Gauss-Bonnet theorem provides a deep and remarkable connection between geometry and topology and has influenced several branches of mathematics and physics. We will see this shortly, but for now we imagine parallel transporting a vector on the spherical surface and move it along the geodesic triangle (see Fig. 2 (b)). It is easy to verify that the vector rotates when it returns to its starting point. The net rotation (mathematically termed as *holonomy*) is equal to the angular excess of the geodesic triangle and is also equal to the total curvature of the triangle.

$$\text{holonomy} = \text{angular excess} = \text{total curvature}. \quad (4)$$

Although we discuss this for a triangular path in our example, a non-trivial holonomy may arise for any closed path. In other words, a vector $v = (a, b)$ acquires a phase (implemented by a rotation $\mathcal{R}(\theta)$) after parallel transport in a closed loop on a surface, i.e.,

$$v = \begin{pmatrix} a \\ b \end{pmatrix} \xrightarrow[|a|^2 + |b|^2 = |a'|^2 + |b'|^2]{\text{parallel transport}} \begin{pmatrix} a' \\ b' \end{pmatrix} = \mathcal{R}(\theta)v. \quad (5)$$

In quantum mechanics, the state of a system can be represented by a vector in Hilbert space. It is therefore natural to consider the effect of parallel transporting a quantum state $|n\rangle$ adiabatically in a closed loop on a curved surface. For example, this could be implemented by suitably varying a parameter R_i of the underlying Hamiltonian $H(\mathbf{R}(t))$ as the state evolves in time. The quantum state $|n\rangle$ rotates or in other words, acquires a phase [that can be referred as $\exp(i\gamma)$] at the end of the adiabatic evolution, where γ is given by [7]

$$\gamma = i \oint_c \langle n | \nabla n \rangle \cdot \mathbf{R}, \quad (6)$$

where the gradient is taken with respect to the parameter \mathbf{R} . This is also known as the Berry phase [7], which can also be expressed as an integral of the Gaussian curvature

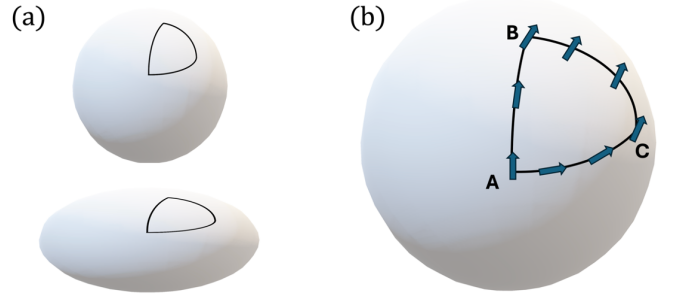


Figure 2. (a) Homeomorphism stretches a sphere to a spheroid but preserves the total curvature. (b) Parallel transporting a vector on the surface of a sphere along the path $A \rightarrow B \rightarrow C \rightarrow A$ results in an angular offset (holonomy).

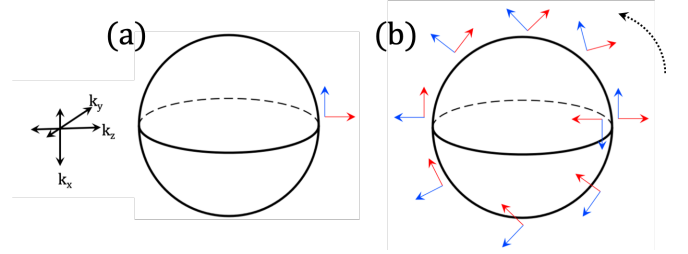


Figure 3. (a) Eigenstates of the Hamiltonian $H_{\mathbf{k}}$ (eigenframe) in Eq. 8 represented by the orthogonal red and blue arrows. (b) Evolving the eigenframe in the direction of the dotted arrow by varying the parameter θ from zero to 2π rotates it by π .

$(\Omega(\mathbf{R}))$ of the surface enclosed inside the closed loop:

$$\gamma = \int \Omega(\mathbf{R}) \cdot d\mathbf{S}, \quad (7)$$

where $\Omega(\mathbf{R}) = i\nabla \times \langle n | \nabla n \rangle$ is also known as the Berry curvature. It turns out that the Berry phase is gauge invariant and is fully consistent with time-dependent quantum evolution. Since γ is invariant under homeomorphism, it is also a topological invariant.

C. Quantum geometry and Weyl fermions

To elucidate the non-trivial role of the Berry phase, we consider a simple two-band Hamiltonian of the form $H_{\mathbf{k}} = \mathbf{k} \cdot \boldsymbol{\sigma}$, where \mathbf{k} is a vector in three-dimensions, and $\boldsymbol{\sigma}$ represents the vector of Pauli matrices.

$$H_{\mathbf{k}} = \mathbf{k} \cdot \boldsymbol{\sigma} = \begin{pmatrix} k_z & k_x - ik_y \\ k_x + ik_y & -k_z \end{pmatrix}. \quad (8)$$

In general, $\boldsymbol{\sigma}$ represents any suitable degree of freedom: orbital, spin, or sublattice, and \mathbf{k} represents any suitable physical parameter. The eigenenergies of the above Hamiltonian are $E_{\mathbf{k}} = \pm k$ and the eigenstates are $|n\rangle^+ = (\cos(\theta/2)e^{-i\phi}, \sin(\theta/2))^T$, $|n\rangle^- =$

$(\sin(\theta/2)e^{-i\phi}, -\cos(\theta/2))^T$, where θ is the polar angle ($\theta = \cos^{-1} k_z/k$), and ϕ is the azimuthal angle ($\tan \phi = k_y/k_x$). We evolve the eigenstates in a fixed gauge varying the polar angle $\theta = \cos^{-1} k_z/k$ (see Fig. 3). As θ varies from zero to 2π , the eigenstates acquire a non-trivial π phase. This is illustrated by the π eigenframe rotation in Fig. 3 (b).

The Berry curvature for the above Hamiltonian is easily evaluated to be

$$\Omega_{\mathbf{k}}^{\pm} = \mp \frac{\hat{\mathbf{k}}}{2k^2}. \quad (9)$$

We note that this is the vector field with a singular point at the origin. This scenario is similar to the electric field generated by a point charge, and thus we can say that the Berry curvature is generated by a monopole at the degeneracy point $\mathbf{k} = 0$ [13, 83, 84]. The degeneracy point thus acts as a source or a sink of the Berry curvature. Integrating the Berry curvature around the degeneracy point equals the number of monopoles (in this case one) in units of 2π . As long as the degeneracy points are protected, homeomorphism on the Hamiltonian by employing small perturbations conserves the number of monopoles or in other words conserves the total curvature by Gauss-Bonnet theorem. This idea lies at the heart of topological protection of quantum states.

As an illustrative comparison, we consider the following Hamiltonian

$$H_{\mathbf{k}} = \begin{pmatrix} k_z^2 - k_x^2 - k_y^2 & 2k_z\sqrt{k_x^2 + k_y^2} \\ 2k_z\sqrt{k_x^2 + k_y^2} & k_x^2 + k_y^2 - k_z^2 \end{pmatrix}, \quad (10)$$

which also has the same energy spectrum $E_{\mathbf{k}} = \pm k$, but the eigenframe in this case rotates by 2π as θ rotates by 2π , entailing a trivial quantum geometry compared to Eq. 8.

Surprisingly, the Hamiltonian in Eq. 8 is identical to the Hamiltonian of Weyl fermions originating in high-energy physics [17]. Weyl fermions here refer to the massless solutions of the Dirac equation [16]. When the mass term in the Dirac equation is set to zero, the Dirac Hamiltonian can be expressed in a block-diagonal form, also known as the Weyl Hamiltonian:

$$H_{\mathbf{k}} = \begin{pmatrix} \mathbf{k} \cdot \boldsymbol{\sigma} & 0 \\ 0 & -\mathbf{k} \cdot \boldsymbol{\sigma} \end{pmatrix} \quad (11)$$

. The diagonal entries in the above Hamiltonian represent Weyl fermions of opposite chiralities (plus/minus or equivalently left/right) [85]. In elementary particle physics neutrinos were initially thought to be Weyl fermions but it was later discovered that neutrinos have a finite mass. So far Weyl fermions have not been observed to exist as elementary particles.

D. Topological Weyl fermions in condensed matter physics

The occurrence of degenerate points in Bloch bands of crystals was first examined by Herring [86] who argued that band degeneracies could occur accidentally in solids. This raised the possibility of observing Weyl fermions as quasiparticle excitations around the degeneracy point where the Berry curvature in the periodic momentum space (Brillouin zone) can become singular. However, it was much later that Nielsen and Ninomiya studied chiral Weyl fermions on a lattice and pointed out that they must occur in pairs [42, 43]. The proof relies on the observation that every source of the Berry curvature vector field must have a sink so that the sum of the indices of the vector field on the Brillouin zone equals zero [87, 88].

The occurrence and topological protection of Weyl fermions as quasiparticles in three spatial dimensions can be understood by considering a general two-band Hamiltonian of the form: [19]

$$H_{\mathbf{k}} = \boldsymbol{\sigma} \cdot \mathbf{f}_{\mathbf{k}} = \begin{pmatrix} f_z(\mathbf{k}) & f_x(\mathbf{k}) - if_y(\mathbf{k}) \\ f_x(\mathbf{k}) + if_y(\mathbf{k}) & -f_z(\mathbf{k}) \end{pmatrix}. \quad (12)$$

In the above Hamiltonian $\mathbf{f}_{\mathbf{k}}$ is a general vector-valued function of crystal-momentum \mathbf{k} . The Hamiltonian can describe the low-energy band structure comprising two bands lying close to the Fermi energy in any spatial dimension d . The energy spectrum is given by $\epsilon_{\mathbf{k}} = \pm \sqrt{f_x(\mathbf{k})^2 + f_y(\mathbf{k})^2 + f_z(\mathbf{k})^2}$. Note that we measure energy relative to the midgap or the band degeneracy point. An energy shift can be easily accomplished by adding a term $\epsilon_0 \mathbb{I}_{2 \times 2}$ in the Hamiltonian. The condition for band-degeneracy is given by $f_x(\mathbf{k})^2 + f_y(\mathbf{k})^2 + f_z(\mathbf{k})^2 = 0$. Let us assume that when $d = 1$, band-degeneracy occurs at points K and K' , i.e., $f_x(K) = f_y(K) = f_z(K) = 0$, and $f_x(K') = f_y(K') = f_z(K') = 0$. This requires three scalar functions of a single variable to intersect at points K and K' . This condition may be satisfied with some amount of fine-tuning (Fig. 4 (a)). We now add a perturbative disorder to the Hamiltonian of the form $V_{\mathbf{k}} = \boldsymbol{\sigma} \cdot \mathbf{g}_{\mathbf{k}}$. The degeneracy condition at point K is then modified to $f_x(K) + g_x(K) = f_y(K) + g_y(K) = f_z(K) + g_z(K) = 0$, and a similar condition exists for the point K' (Fig. 4 (d)). In general, this is very hard to satisfy because of the random nature of the disorder. The band degeneracy points are therefore not protected and the degeneracy can be lifted by infinitesimal disorder.

In two spatial dimensions ($d = 2$), the band-degeneracy condition at points $\mathbf{K} = (K_x, K_y)$ and $\mathbf{K}' = (K'_x, K'_y)$ is $f_x(\mathbf{K}) = f_y(\mathbf{K}) = f_z(\mathbf{K}) = 0$, and $f_x(\mathbf{K}') = f_y(\mathbf{K}') = f_z(\mathbf{K}') = 0$. This requires three curves to intersect precisely at two points, which again may be realized by fine-tuning (Fig. 4 (b)). Small perturbations can move the curves (Fig. 4 (e)) on the plane and thus the degenerate point is again not protected. Moving to $d = 3$, the band-degeneracy condition at point $\mathbf{K} = (K_x, K_y, K_z)$ and $\mathbf{K}' = (K'_x, K'_y, K'_z)$ is $f_x(\mathbf{K}) = f_y(\mathbf{K}) = f_z(\mathbf{K}) = 0$,

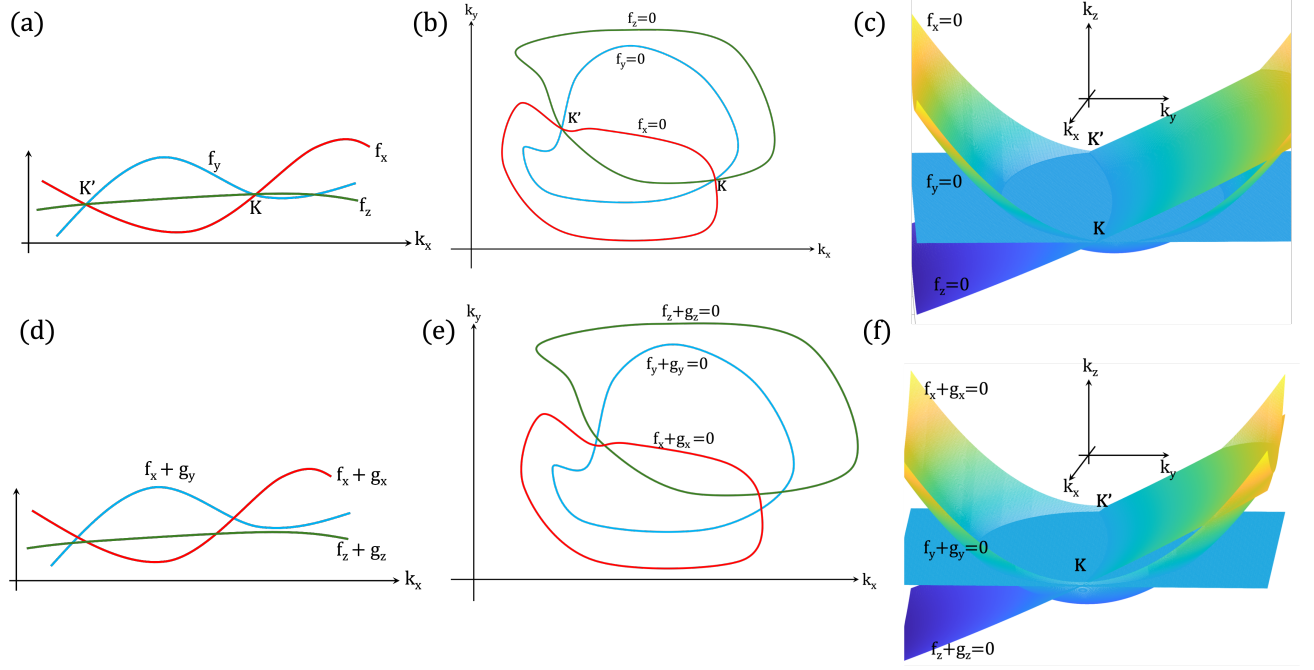


Figure 4. (a) Degenerate points in $d = 1$ correspond to three functions intersecting at two points K and K' . (b) When $d = 2$, this condition is modified to three intersecting curves on a plane. (c) When $d = 3$, the condition modifies to three intersecting surfaces meeting at two points K and K' . (d) and (e) Small perturbations ($\mathbf{g}_{\mathbf{k}}$) move the curves and the fine-tuned Weyl points are destroyed. (f) Small perturbations move the surfaces and the Weyl points shift in momentum-space but remain protected.

and a similar condition for \mathbf{K}' . This condition amounts to three intersecting surfaces meeting at two points (Fig. 4 (c)). Perturbations will change the surfaces and modify the degeneracy conditions (Fig. 4 (f)). However, the degenerate points are just shifted in momentum space, unless the two points move closer and annihilate. Band touching is therefore robust in three spatial dimensions.

Having found protected degenerate points in a three-dimensional solid, we can now expand the Hamiltonian in Eq. 12 around the point \mathbf{K} as:

$$H_{\mathbf{k}} = \begin{pmatrix} \nabla f_z(\mathbf{K}) & \nabla f_x(\mathbf{K}) - i\nabla f_y(\mathbf{K}) \\ \nabla f_x(\mathbf{K}) + i\nabla f_y(\mathbf{K}) & -\nabla f_z(\mathbf{K}) \end{pmatrix} \cdot \mathbf{k}, \quad (13)$$

where \mathbf{k} is now measured relative to the \mathbf{K} point. The above Hamiltonian can be expressed as:

$$H_{\mathbf{k}} = \sum_{i=x,y,z} \sum_{j=x,y,z} v_{ij} k_i \sigma_j, \quad (14)$$

where $v_{ij} = \partial_i f_j$. This is the general form of the Weyl fermion Hamiltonian near the Weyl node. The nodal point is protected by the *chirality* quantum number χ , given by $\chi = \text{sign}(\det[v_{ij}])$, which is also equal to the flux of the Berry curvature of a Bloch band:

$$\chi = \frac{1}{2\pi} \oint \Omega_{\mathbf{k}} \cdot d\mathbf{S}. \quad (15)$$

Here the integral is over the Fermi surface enclosing the nodal point and $d\mathbf{S}$ is the area element. In an appropriate frame of reference we may write $v_{ij} = v_i \delta_{ij}$, and obtain a more familiar form of the Weyl Hamiltonian $H_{\mathbf{k}} = \hat{\mathbf{k}} \cdot \boldsymbol{\sigma}$, where $\hat{\mathbf{k}} = (v_x k_x, v_y k_y, v_z k_z)$ similar to Eq. 8. A similar expansion can be done around the \mathbf{K}' point. Although $H_{\mathbf{k}} = \hat{\mathbf{k}} \cdot \boldsymbol{\sigma}$ is anisotropic, much of the fundamental Weyl physics can be understood by considering the isotropic version $H_{\mathbf{k}} = \mathbf{k} \cdot \boldsymbol{\sigma}$. The Berry curvature of a pair of Weyl nodes is schematically depicted in Fig. 5.

E. Chiral anomaly of Weyl fermions

Chiral anomaly (CA) refers to the non-conservation of the left and right-handed chiral Weyl fermions in the presence of external gauge fields. It is also known as the Adler-Bell-Jackiw (ABJ) anomaly and originates in high energy physics [40]. This non-conservation of chiral charges results in a nonvanishing chiral current that may lead to chirality-dependent transport. In the context of WSMs, CA can be verified experimentally through the measurement of (but not limited to) magnetoconductance [45], Hall conductance [25, 89], thermoelectric [50] and Nernst effects [52], optical processes [73], and non-local transport [90].

Nielsen and Ninomiya were among the first to investigate chiral anomaly in crystals [42, 43]. They derived the chiral anomaly or the ABJ anomaly from a physical

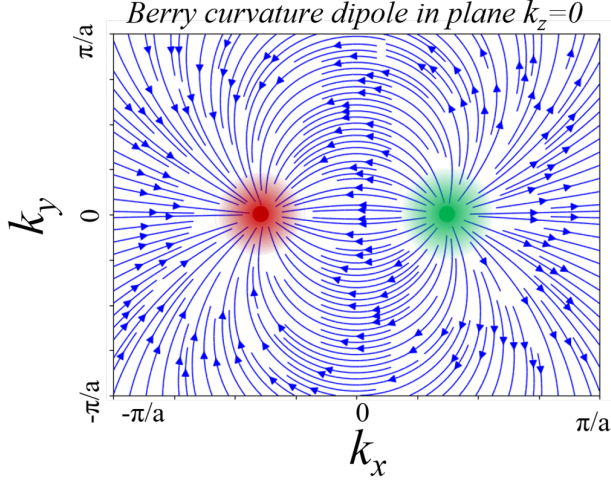


Figure 5. Schematic diagram to show the Berry curvature field lines in momentum space for $k_z = 0$. The red and green regions correspond to two points having opposite chirality. Here, a is the lattice constant of the system.

point of view as the production of Weyl particles, and show that there is an absence of the net production of particles for local chiral invariant theories regularized on a lattice. They showed that fermion systems in lattice gauge theories are similar to electron systems in crystals, so as a result there should exist a mechanism in crystals that is similar to the ABJ anomaly. When two energy bands have point-like degeneracies, the Weyl particles can move from one degeneracy to the other in the presence of parallel electric and magnetic fields leading to a large longitudinal positive magnetoconductance [91], which is a manifestation of the anomaly in crystals. The exact sign of LMC is more nuanced and we discuss this in detail in a later section.

We present a brief overview of CA with help of a simple Landau-levels picture [18]. In Fig. 6 (a), we sketch a WSM of finite size with volume $V = l_x l_y l_z$, subject to external electric (\mathbf{E}) and magnetic field (\mathbf{B}). We quantize the levels in presence of an external magnetic field. The Corresponding energy dispersion is plotted in Fig. 6 (b), where the energy levels disperse along the direction of magnetic field \mathbf{B} . Except $n = 0$ level, all the Landau levels are degenerate with degeneracy $g = 2\pi e B l_x l_y / \hbar$. The zeroth Landau level is chiral in nature and its direction of dispersion depends upon the chirality χ of Weyl node. The general form of the dispersion may be explicitly written as:

$$\epsilon(\mathbf{k}) = \begin{cases} v_F \text{sign}(n) \sqrt{2\hbar|n|eB + (\hbar k_z)^2}, & n = \pm 1, \pm 2, \dots \\ -\chi \hbar v_F k_z, & n = 0. \end{cases} \quad (16)$$

We will assume that $\mu \ll v_F \sqrt{\hbar e B}$. For this case one

focuses only on the zeroth Landau level physics; this is also dubbed as the *quantum limit*. As depicted in Fig. 6 (a), for $\mathbf{E} = E\hat{z}$ and $\gamma = \pi/2$, i.e., $\mathbf{B} = B\hat{z}$, all the states are forced to mobilize along \hat{z} -direction: $d\mathbf{k}/dt = (-e/\hbar)\mathbf{E}$. Therefore, electrons in the zeroth Landau level at valley $\chi = 1$ move towards the left and at valley $\chi = -1$ towards the right. This mobilization of states appears as the disappearance of electrons from the band having a positive slope and reappearance to the band having a negative slope through a hidden channel marked by a black dotted curve in Fig. 6(b). This process leads to non-conservation of charge at a particular chiral Landau level. In conclusion, chiral Landau levels have 1d chiral anomaly which results in an imbalance of the population of charges at two valleys having opposite chiralities. The rate of change of charge particle at valley having chirality χ is given by:

$$\frac{\partial Q_{\hat{z}}^{\chi}}{\partial t} = e\chi l_z \frac{|\dot{\mathbf{k}}|}{2\pi} = -2\pi e^2 \chi l_z \frac{|\mathbf{E}|}{\hbar}. \quad (17)$$

Including degeneracy of the Landau levels ($g = 2\pi e B l_x l_y / \hbar$), this is generalised as follows:

$$\frac{\partial Q_{3D}^{\chi}}{\partial t} = g \frac{\partial Q_{\hat{z}}^{\chi}}{\partial t} = -\frac{e^3}{4\pi^2 \hbar^2} l_x l_y l_z \mathbf{E} \cdot \mathbf{B}. \quad (18)$$

We will see in the next section how the $\mathbf{E} \cdot \mathbf{B}$ term appears in the semiclassical equations of motion and allows us to study CA and CA-assisted transport through the Bloch-Boltzmann formalism.

II. ELECTRON TRANSPORT IN WEYL FERMIONS

A. Maxwell-Boltzmann transport theory of Weyl fermions

Electrons in solids are influenced by the periodic lattice potential of ions situated at well-defined basis points. The electronic conductivity of solids therefore must account for this periodic potential. A solution to this problem was given by Bloch [92] and thus noninteracting electrons in periodic potential are dubbed as Bloch electrons. Bloch electrons conserve the crystal momentum and have plane-wave solutions modulated by a periodic function: $\psi_{\mathbf{k}}^n(\mathbf{r}) = e^{i\mathbf{k} \cdot \mathbf{r}} u_{\mathbf{k}}^n(\mathbf{r})$, where n is the band index. Extending Sommerfeld's theory to nonequilibrium cases in the presence of external perturbations, one then explores the conduction of solids. Here, the dynamics of Bloch electron wavepackets are considered classical. These classical equations describe the behavior of the wave packet of electron levels as shown in Fig. 7, which is forced to obey the uncertainty principle. The equations of motion to track the evolution of the position (\mathbf{r}) and wave vector (\mathbf{k}) of an electron in an external electromagnetic field (\mathbf{E}

and \mathbf{B}) are:

$$\begin{aligned}\dot{\mathbf{r}} &\equiv \mathbf{v} = \frac{1}{\hbar} \frac{\partial \epsilon(\mathbf{k})}{\partial \mathbf{k}}, \\ \hbar \dot{\mathbf{k}} &= e(\mathbf{E} + \dot{\mathbf{r}} \times \mathbf{B}).\end{aligned}\quad (19)$$

As we noted earlier, Weyl fermions in solids, due to the nontrivial topology of the bands, possess a Berry curvature which modifies the above equation to the one presented in the following equation [93]:

$$\begin{aligned}\dot{\mathbf{r}}^\chi &= \mathcal{D}^\chi \left(\frac{e}{\hbar} (\mathbf{E} \times \boldsymbol{\Omega}^\chi) + \frac{e}{\hbar} (\mathbf{v}^\chi \cdot \boldsymbol{\Omega}^\chi) \mathbf{B} + \mathbf{v}_\mathbf{k}^\chi \right) \\ \dot{\mathbf{p}}^\chi &= -e \mathcal{D}^\chi \left(\mathbf{E} + \mathbf{v}_\mathbf{k}^\chi \times \mathbf{B} + \frac{e}{\hbar} (\mathbf{E} \cdot \mathbf{B}) \boldsymbol{\Omega}^\chi \right),\end{aligned}\quad (20)$$

where $\boldsymbol{\Omega}^\chi = -\chi \mathbf{k} / 2k^3$ is the Berry curvature of Weyl fermions, and $\mathcal{D}^\chi = (1 + e \mathbf{B} \cdot \boldsymbol{\Omega}^\chi / \hbar)^{-1}$. The self-rotation of the Bloch wave packet, which has a finite spread in the phase space, also gives rise to an orbital magnetic moment (OMM) $\mathbf{m}_\mathbf{k}^\chi$ [13]. In the presence of a magnetic field, the OMM shifts the energy dispersion as $\epsilon_\mathbf{k}^\chi \rightarrow \epsilon_\mathbf{k}^\chi - \mathbf{m}_\mathbf{k}^\chi \cdot \mathbf{B}$. Note that we have added the chirality index χ to distinguish Weyl fermions of different flavors.

Returning to the quasiclassical formalism, it shows that a Bloch electron wavepacket has nonvanishing band velocity ($\mathbf{v}_\mathbf{n}$) proportional to $(\partial \epsilon(\mathbf{k}) / \partial \mathbf{k})$. So a perfect solid has infinite conductivity. The inclusion of the wave nature of the electron justifies this as constructive interference of scattered waves from an array of periodic potentials allowing it to propagate through solids without attenuation [92]. Since no crystal structure is perfect, imperfection leads to the degradation of current giving rise to finite conductivity. Using the semiclassical Boltzmann formalism, one can investigate charge transport in the presence of perturbative electric and magnetic fields and evaluate the conductivity. For spatially uniform fields, the formalism assumes the presence of a distribution function $f_\mathbf{k}$ of electrons which reduces to the Fermi-Dirac distribution in equilibrium. The nonequilibrium distribution function satisfies the following equation: [94]

$$\frac{\partial f_\mathbf{k}}{\partial t} + \dot{\mathbf{r}}_\mathbf{k} \cdot \nabla_\mathbf{r} f_\mathbf{k} + \dot{\mathbf{k}} \cdot \nabla_\mathbf{k} f_\mathbf{k} = I_{\text{coll}}[f_\mathbf{k}]. \quad (21)$$

We assume $f_\mathbf{k} = f_{0\mathbf{k}} + g_\mathbf{k}$, where $f_{0\mathbf{k}}$ is the standard Fermi-Dirac distribution and $g_\mathbf{k}$ is the deviation due to external fields. Perturbation theory allows us to go up to the order of choice to discuss the higher orders of different electromagnetic responses of the materials. When restricted to the first order in \mathbf{E} , then $g_\mathbf{k} \propto \mathbf{E}$. The right-hand side in Eq. 21 (the collision integral term) accounts for the relaxation processes in the system. The simplest approach adapted in the literature is the ‘relaxation time approximation’ with momentum-independent

constant scattering time that assumes

$$I_{\text{coll}}[f_\mathbf{k}] = -\frac{g_\mathbf{k}}{\tau}, \quad (22)$$

where τ is the scattering time. Once the distribution function is obtained, conductivity can be straightforwardly obtained via the following relation:

$$\mathbf{j} = -e \sum_\mathbf{k} \dot{\mathbf{r}}_\mathbf{k} g_\mathbf{k}. \quad (23)$$

In the case of Weyl fermions, we need to consider the scattering of an electron from an occupied state with momentum \mathbf{k} and chirality χ to an unoccupied state with momentum \mathbf{k}' and chirality χ' . This leads to two processes: (i) if $\chi = \chi'$, this is termed as intranode (or intravalley) scattering, referring to the preservation of the chirality index of the particle, (ii) when $\chi \neq \chi'$, this is termed as internode (or intervalley) scattering referring to breaking of the chirality index. Therefore one typically needs to consider two scattering times: (i) τ_{inter} , which is the internode scattering time, and (ii) τ_{intra} , which is the intranode scattering time. Furthermore, the distribution functions at both nodes must have a chirality index as well. The collision integral can therefore be expressed as [45, 49]

$$I_{\text{coll}}[f_\mathbf{k}^\chi] = -\frac{f_\mathbf{k}^\chi - f_\mathbf{k}^{\chi' \neq \chi}}{\tau_{\text{inter}}} - \frac{f_\mathbf{k}^\chi - f_\mathbf{k}^{\chi' = \chi}}{\tau_{\text{intra}}}. \quad (24)$$

The internode scattering mechanism successfully captures the essence of chiral anomaly-induced transport phenomena as first pointed out by Son and Spivak [45]. It predicts *negative* longitudinal magnetoresistance, which was initially considered a definitive signature of the manifestation of chiral anomaly in solids. Recent works [56, 57, 67–69] have evolved this understanding, which we will discuss later.

The linear response formalism for computing conductivity [95], presupposes a timescale denoted by τ_ϕ , which signifies the interactions between the system and the external electric field. This timescale reflects the inelastic exchange of energy at a rate of τ_ϕ . The rate is ideally assumed to be zero, meaning that τ_ϕ is presumed to be the longest among all relevant timescales. For weakly disordered Weyl semimetals, particularly when Landau quantization of energy levels becomes significant under intense magnetic fields, chiral anomaly becomes apparent through a positive contribution to the longitudinal magnetoconductance, expressed as $\mathbf{j} \propto B(\mathbf{E} \cdot \mathbf{B})$. The current flow is constrained by the internode scattering time (τ_{inter}), representing the timescale at which electrons scatter across the nodes and alter their chirality. Consequently, while the chiral charge isn’t conserved, the global charge is conserved. For the linear response formalism to be valid, τ_{inter} must significantly exceed τ_ϕ . However, when intranode scattering is the dominant scattering mechanism, the conservation of chiral charge along

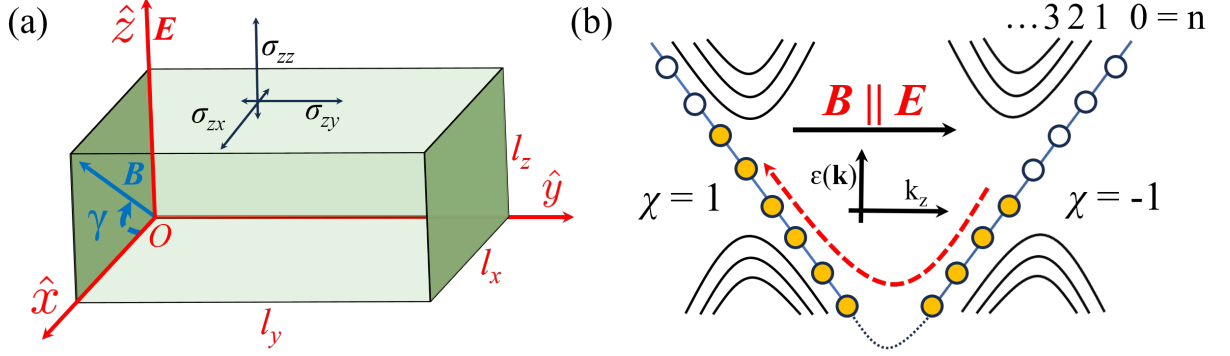


Figure 6. (a) Schematic illustration of the experimental setup to measure different conductivity responses of 3D WSMs under external electric and magnetic fields. $V = l_x l_y l_z$ is sample volume, γ is to tune the direction of the magnetic field which is very helpful to study the chiral magnetic effect as chiral current is proportional to $\mathbf{E} \cdot \mathbf{B}$. (b) Landau level picture of the dispersion of WSMs having pair of Weyl nodes with chirality $\chi = \pm 1$. Occupancy of the chiral Landau level ($n = 0$) has been marked by the yellow circles and it is the only one to participate in the chiral pumping process under parallel electric and magnetic fields.

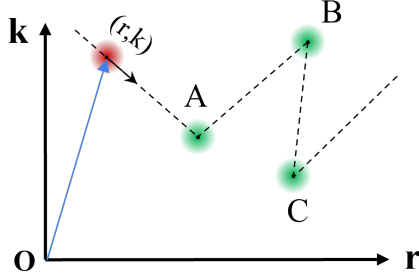


Figure 7. Diagrammatic depiction of the classical route of a Bloch electron wavepacket in the phase space, which is governed by the classical equations of motion i.e., Eq. 20. The position is indicated by the blue arrow and can be expressed as the coordinate (\mathbf{r}, \mathbf{k}) . The direction of motion is shown by the black arrow on the dotted route. Impurity sites that are naturally present in the system are denoted by A, B, and C. This semiclassical method enables us to follow an electron between two consecutive collisions.

with global charge becomes important, and the calculations need to be re-examined.

When magnetic fields are weak and quantization of levels is unimportant, Son and Spivak [45] predicted internode scattering induced positive longitudinal magnetoelectricity (LMC) in Weyl semimetals (WSMs) via the semiclassical Boltzmann approach. Later on, several studies proposed that positive LMC can arise solely from intranode scattering, as evidenced by a coupling term $\mathbf{E} \cdot \mathbf{B}$ (Eq. 20) incorporated into the semiclassical equations of motion [49–56]. This suggests that positive LMC can occur in WSMs even in the limit where $\tau_{\text{inter}}/\tau_{\text{intra}} \rightarrow \infty$. Notably, none of the studies differentiate between two parameter regimes: $\tau_{\text{intra}} \ll \tau_\phi \ll \tau_{\text{inter}}$ and $\tau_{\text{intra}} \ll \tau_{\text{inter}} \ll \tau_\phi$. This distinction carries significant consequences, as the chiral charge is conserved in the former case, while the latter indicates global charge

conservation, occurring on a timescale larger than the intravalley timescale τ_{intra} but smaller than τ_ϕ . The assertion that intranode scattering alone can yield positive LMC assumes that $\tau_{\text{intra}} \ll \tau_\phi \ll \tau_{\text{inter}}$, which is incorrect. This issue was recently resolved in Ref. [67] where Sharma *et al.* calculated transport properties including LMC correctly for various possible values of the parameters τ_{intra} , τ_{inter} , and τ_ϕ .

Furthermore, in the same work [67], Sharma *et al.*, showed that a constant relaxation time approximation in Weyl fermions is inherently inconsistent with charge conservation. This is understood by the following illustrative example. Consider one Weyl node with chirality χ and the following low-energy Hamiltonian: $H_{\mathbf{k}} = \chi \hbar v_F \mathbf{k} \cdot \boldsymbol{\sigma}$. The steady-state Boltzmann equation takes the following form in the relaxation-time approximation [67]:

$$e \mathcal{D}_{\mathbf{k}}^{\chi} \left(-\frac{\partial f_{0\mathbf{k}}}{\partial \epsilon_{\mathbf{k}}} \right) \left(\mathbf{v}_{\mathbf{k}}^{\chi} + \frac{e}{\hbar} \mathbf{B} (\boldsymbol{\Omega}_{\mathbf{k}}^{\chi} \cdot \mathbf{v}_{\mathbf{k}}^{\chi}) \right) \cdot \mathbf{E} = -\frac{g_{\mathbf{k}}^{\chi}}{\tau_{\mathbf{k}}} \quad (25)$$

Charge conservation suggests that $\sum_{\mathbf{k}} g_{\mathbf{k}}^{\chi} = 0$. When both

\mathbf{E} and \mathbf{B} are parallel to the z -axis, the charge conservation equation reduces to:

$$\int \tau^{\chi}(\theta) \left(v_z^{\chi} + \frac{e}{\hbar} B (\boldsymbol{\Omega}_{\mathbf{k}}^{\chi} \cdot \mathbf{v}_{\mathbf{k}}^{\chi}) \right) \frac{k^3(\theta) \sin \theta}{|\mathbf{v}_{\mathbf{k}}^{\chi} \cdot \mathbf{k}|} d\theta = 0. \quad (26)$$

Here, all quantities in the integrand are evaluated on the Fermi surface at zero temperature. A common simplification often utilized is to assume that the scattering time is independent of momentum \mathbf{k} , denoted as $\tau^{\chi}(\theta) = \tau^{\chi}$ [49–55]. However, it can be readily observed from Eq. 26 that when $\tau^{\chi}(\theta)$ is independent of θ , the left-hand side of the equation does not reduce to zero. Therefore, a momentum-independent scattering time is inherently incompatible with particle number conservation. It is important to go beyond the constant relaxation-time approximation, which is reviewed next.

B. Beyond constant relaxation-time approximation

To correctly study magnetotransport, going beyond the constant relaxation-time approximation is inevitable [56, 57, 67–69]. We therefore write the collision integral as:

$$I_{coll}[f_{\mathbf{k}}^{\chi}] = \sum_{\chi' \mathbf{k}'} W_{\mathbf{k}\mathbf{k}'}^{\chi\chi'} (f_{\mathbf{k}'}^{\chi'} - f_{\mathbf{k}}^{\chi}), \quad (27)$$

where the scattering rate $W_{\mathbf{k}\mathbf{k}'}^{\chi\chi'}$ is evaluated in the first Born approximation (Fermi's golden rule) as:

$$W_{\mathbf{k}\mathbf{k}'}^{\chi\chi'} = \frac{2\pi n}{\mathcal{V}} |\langle u^{\chi'}(\mathbf{k}') | U_{\mathbf{k}\mathbf{k}'}^{\chi\chi'} | u^{\chi}(\mathbf{k}) \rangle|^2 \delta(\epsilon^{\chi'}(\mathbf{k}') - \epsilon_F). \quad (28)$$

In the above expression n is the impurity concentration, \mathcal{V} is the system volume, $|u^{\chi}(\mathbf{k})\rangle$ is the Weyl spinor wave function obtained from diagonalization of the Hamiltonian in Eq. 8, $U_{\mathbf{k}\mathbf{k}'}^{\chi\chi'}$ is the scattering potential, and ϵ_F is the Fermi energy. We choose $U_{\mathbf{k}\mathbf{k}'}^{\chi\chi'}$ to model non-magnetic point-like impurities. So, in general $U_{\mathbf{k}\mathbf{k}'}^{\chi\chi'} = U^{\chi\chi'} \sigma_0$, where σ_0 is an identity matrix, and the parameter $U^{\chi\chi'}$ can distinguish the intervalley and intravalley scattering. We do not discuss magnetic impurities here but a recent work of ours discusses that as well [70].

Using Eq. 20, 27 and keeping terms up to linear order in the applied fields, the Boltzmann transport equation can be written as:

$$\begin{aligned} & \left[\left(\frac{\partial f_0^{\chi}}{\partial \epsilon_{\mathbf{k}}^{\chi}} \right) \mathbf{E} \cdot \left(\mathbf{v}_{\mathbf{k}}^{\chi} + \frac{e\mathbf{B}}{\hbar} (\boldsymbol{\Omega}_{\mathbf{k}}^{\chi} \cdot \mathbf{v}_{\mathbf{k}}^{\chi}) \right) \right] \\ &= -\frac{1}{e\mathcal{D}^{\chi}} \sum_{\chi'} \sum_{\mathbf{k}'} W_{\mathbf{k}\mathbf{k}'}^{\chi\chi'} (g_{\mathbf{k}'}^{\chi'} - g_{\mathbf{k}}^{\chi}). \end{aligned} \quad (29)$$

This is a vector equation that can be simplified by fixing the electric field along a particular direction. We fix the electric field along increasing x -direction and the magnetic field can be rotated in xz -plane. Therefore, $\mathbf{E} = E(0, 0, 1)$ and $\mathbf{B} = B(\cos \gamma, 0, \sin \gamma)$, i.e., for $\gamma = \pi/2$ both the fields are parallel. By tuning the γ we can control the component of the magnetic field along the electric field, i.e. $\mathbf{E} \cdot \mathbf{B}$ term in the Eq. 20 which is responsible for the chiral anomaly. This geometry is useful for studying the different electromagnetic responses, especially the planar Hall effect and longitudinal magnetoconductance (we will return to this later). In this geometry, only the z -component of $\boldsymbol{\Lambda}_{\mathbf{k}}^{\chi}$ is relevant, so Eq. 29 reduces to

$$\mathcal{D}^{\chi} \left[v_{\mathbf{k}}^{\chi,z} + \frac{eB \sin \gamma}{\hbar} (\mathbf{v}_{\mathbf{k}}^{\chi} \cdot \boldsymbol{\Omega}_{\mathbf{k}}^{\chi}) \right] \sum_{\chi' \mathbf{k}'} W_{\mathbf{k}\mathbf{k}'}^{\chi\chi'} (\Lambda_{\mathbf{k}'}^{\chi'} - \Lambda_{\mathbf{k}}^{\chi}). \quad (30)$$

We define a valley scattering rate:

$$\frac{1}{\tau_{\mathbf{k}}^{\chi}(\theta, \phi)} = \sum_{\chi'} \mathcal{V} \int \frac{d^3 \mathbf{k}'}{(2\pi)^3} (\mathcal{D}_{\mathbf{k}'}^{\chi'})^{-1} W_{\mathbf{k}\mathbf{k}'}^{\chi\chi'}. \quad (31)$$

On the right-hand side of the above equation, there is a sum over the chirality index χ which can run over multiple flavors. For example, time reversal symmetry broken WSM has a minimum of two Weyl cones, so the summation is over two nodes. But, inversion symmetry broken WSM has a minimum of four Weyl cones so it runs for all four nodes. The overlap of the Bloch wave-functions $\langle u^{\chi'}(\mathbf{k}') | U_{\mathbf{k}\mathbf{k}'}^{\chi\chi'} | u^{\chi}(\mathbf{k}) \rangle^2$ in Eq. 28 is given by the following expression, $\mathcal{G}^{\chi\chi'}(\theta, \phi) = [1 + \chi\chi'(\cos \theta \cos \theta' + \sin \theta \sin \theta' \cos \phi \cos \phi' + \sin \theta \sin \theta' \sin \phi \sin \phi')]$. The overlap of the wave function includes the transition probabilities between fermions of the same chiralities as well as different chiralities. Taking Berry phase into account and the corresponding change in the density of states, $\sum_{\mathbf{k}} \rightarrow \mathcal{V} \int \frac{d^3 \mathbf{k}}{(2\pi)^3} \mathcal{D}^{\chi}(k)$, Eq. 30 becomes:

$$\begin{aligned} h_{\mu}^{\chi}(\theta, \phi) + \frac{\Lambda_{\mu}^{\chi}(\theta, \phi)}{\tau_{\mu}^{\chi}(\theta, \phi)} = \\ \sum_{\chi'} \mathcal{V} \int \frac{d^3 \mathbf{k}'}{(2\pi)^3} \mathcal{D}^{\chi'}(k') W_{\mathbf{k}\mathbf{k}'}^{\chi\chi'} \Lambda_{\mu}^{\chi'}(\theta', \phi') \end{aligned} \quad (32)$$

Here, the explicit form of the h_{μ}^{χ} is $h_{\mu}^{\chi}(\theta, \phi) = \mathcal{D}^{\chi}[v_{z,\mathbf{k}}^{\chi} + eB \sin \gamma (\boldsymbol{\Omega}_{\mathbf{k}}^{\chi} \cdot \mathbf{v}_{\mathbf{k}}^{\chi})]$ and is independent of the nature of the impurity sites. The momentum integral in Eq. 32 has to be evaluated at the Fermi surface, and for that one has to change the momentum integration into the energy integration. In the zero temperature limit, for a constant Fermi energy surface, the Eq. 31 and RHS of Eq. 32 is reduced to the integration over θ' and ϕ' :

$$\frac{1}{\tau_{\mu,i}^{\chi}(\theta, \phi)} = \mathcal{V} \sum_{\chi'} \Pi^{\chi\chi'} \iint \frac{(k')^3 \sin \theta'}{|\mathbf{v}_{\mathbf{k}'}^{\chi'} \cdot \mathbf{k}^{\chi'}|} d\theta' d\phi' \mathcal{G}^{\chi\chi'} (\mathcal{D}_{\mathbf{k}'}^{\chi'})^{-1} \quad (33)$$

The parameter τ in this expression is independent of radial distance but is dependent on the angles θ, ϕ , and the nature of the impurity sites. By using this expression for τ , and Eq. 28 the right-hand side of the Eq. 32 takes the form:

$$\begin{aligned} & [d^{\chi} + a^{\chi} \cos \phi + b^{\chi} \sin \theta \cos \phi + c^{\chi} \sin \theta \sin \phi] \\ &= \sum_{\chi'} \mathcal{V} \Pi^{\chi\chi'} \iint f^{\chi'}(\theta', \phi') d\theta' d\phi' \\ &\times [d^{\chi'} - h_{\mathbf{k}'}^{\chi'} + a^{\chi'} \cos \theta' + b^{\chi'} \sin \theta' \cos \phi' + c^{\chi'} \sin \theta' \sin \phi'], \end{aligned} \quad (34)$$

where $\Pi^{\chi\chi'} = N |U^{\chi\chi'}|^2 / 4\pi^2 \hbar^2$, $f^{\chi}(\theta, \phi) = \frac{(k)^3}{|\mathbf{v}_{\mathbf{k}}^{\chi} \cdot \mathbf{k}^{\chi}|} \sin \theta (\mathcal{D}_{\mathbf{k}}^{\chi})^{-1} \tau_{\mu}^{\chi}(\theta, \phi)$ and the exact form of

the ansatz is $\Lambda_{\mathbf{k}}^{\chi} = [d^{\chi} - h_{\mathbf{k}'}^{\chi} + a^{\chi} \cos \phi + b^{\chi} \sin \theta \cos \phi + c^{\chi} \sin \theta \sin \phi] \tau_{\mu}^{\chi}(\theta, \phi)$. When the aforementioned equation is explicitly put out, it appears as seven simultaneous equations that must be solved for eight variables. The particle number conservation provides the final restriction:

$$\sum_{\chi} \sum_{\mathbf{k}} g_{\mathbf{k}}^{\chi} = 0. \quad (35)$$

For the eight unknowns $(d^{\pm 1}, a^{\pm 1}, b^{\pm 1}, c^{\pm 1})$, the equations 34 and 35 are simultaneously solved with Eq. 33. Note that if we have more than two flavors of Weyl fermions, the number of equations and unknowns will increase. For example, in the case of inversion asymmetric WSMs, we need to numerically solve sixteen equations for sixteen coefficients [67, 68].

III. ANOMALOUS TRANSPORT RESPONSES

A. Longitudinal magnetoconductance

Initial calculations suggested that CA always resulted in a positive LMC [45, 96–100] or equivalently, negative magnetoresistance. Son & Spivak [45] showed that a Weyl metal, that has Weyl points immersed inside the Fermi surface can have a chiral anomaly induced large negative magnetoresistance [45]. The explanation offered was semiclassical where the mean free path is short compared to the magnetic length and Landau quantization of levels is irrelevant. As a result, the electron transport properties were studied using the Boltzmann equation, predicting the electric conductivity to depend quadratically on the applied magnetic field. Burkov [101] arrived at the same conclusion using a microscopic theory of diffusive transport. A later work by Spivak & Andreev [100] also explained the occurrence of large negative magnetoconductance in Weyl metals due to CA using the semiclassical Boltzmann transport theory. According to them, negative magnetoresistance in a conductor in weak fields can easily be explained with Boltzmann transport theory by invoking Berry curvature without which the magnetoresistance remains positive. A lot of experimental observations of possible WSM candidates have shown large magnetoresistance consistent with the above studies [36, 59, 61–63]. While correct in spirit, these theoretical works assume a momentum-independent relaxation time, which as we show earlier, is an incorrect assumption for Weyl fermions.

It has come to light that positive longitudinal magnetoconductance doesn't exclusively confirm the presence of chiral anomaly in Weyl semimetals. Notably, positive LMC can manifest even without Weyl nodes, as observed in ultraclean PdCoO₂ [102–104]. Furthermore, experimental studies indicate that the jetting effect can yield false positive LMC due to extrinsic factors, irrespective of the presence of any anomaly [97]. However, a recent

work [105] demonstrates that meticulous measurement of voltage drops along the sample's mid ridge and edges can mitigate this effect. Theoretically, it is now also established that Weyl nodes don't invariably lead to positive LMC. In strong magnetic fields, where one needs to consider effects due to Landau quantization, LMC can be both positive or negative for short-range impurities, while it is typically positive for long-range charged impurities [32, 47, 106–110]. In the regime of weak magnetic fields, it was conventionally understood that LMC is positive [51, 65, 71, 80, 91, 100, 111, 112]. However, a recent works [56, 57, 67–69] reveal that LMC can be negative with sufficiently strong intervalley scattering, especially when the effects of orbital magnetic moment (OMM) and are considered beyond the constant relaxation-time approximation.

Knoll *et al.* [56] studied the CA-induced LMC in WSMs using the semiclassical theory, including the effects of the anomalous orbital magnetic moment and going beyond the constant relaxation-time approximation. They explain that the anomalous shift in the energy due to the OMM, which changes the geometry of the Fermi surface from spherical to egg-shape, along with the relative strength of the intervalley scattering, is crucial in determining the sign of LMC in the weak-field limit. For small values of relative intervalley scattering strength, LMC is found positive. If the relative intervalley scattering strength is increased further, there is a sign change of LMC from positive to negative at some critical value of α . This is also highlighted in Fig. 11. Similar conclusions were reported by Sharma *et al.* in Ref. [57].

1. Single node LMC

Sharma *et al.* [67] revisited this problem and first evaluated LMC for strictly zero internode scattering. We briefly summarize this here. Before proceeding with the calculation, we point out that we adopt the following Weyl Hamiltonian near a nodal point of chirality χ :

$$H_{\mathbf{k}} = \chi \hbar v_F \boldsymbol{\sigma} \cdot \mathbf{k}, \quad (36)$$

where we have inserted the factors of Fermi velocity and the reduced Planck's constant to be dimensionally consistent.

In this scenario, it is enough to compute the outcome for just one isolated Weyl node, and then sum the contributions of both the nodes. Given the inadequacy of the momentum-independent relaxation time, we opt for the collision integral to be:

$$\mathcal{I}_{\text{coll}}[g_{\mathbf{k}}^{\chi}] = \sum_{\mathbf{k}'} (\Lambda_{\mathbf{k}}^{\chi} - \Lambda_{\mathbf{k}'}^{\chi}) W_{\mathbf{k}\mathbf{k}'}^{\chi\chi} (-\partial g_0 / \partial \epsilon_k) eE. \quad (37)$$

The unknown function $\Lambda_{\mathbf{k}}^{\chi}$ is assumed to be

$$\Lambda_{\mathbf{k}}^{\chi} = (f_{\mathbf{k}}^{\chi} - h_{\mathbf{k}}^{\chi}) \tau_{\mathbf{k}}^{\chi}, \quad (38)$$

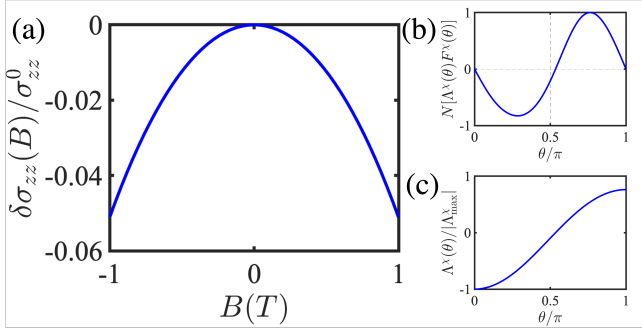


Figure 8. (a) LMC for an isolated Weyl node is always negative due to chiral charge conservation. (b) $\Lambda^\chi(\theta)$ between 0 and π at $B = 1T$. (c) The corresponding normalized deviation in the distribution function (proportional to g_k^χ), which integrates to zero. Here $\chi = 1$. Figure adapted from Ref. [67].

where $h_{\mathbf{k}}^\chi = \mathcal{D}_{\mathbf{k}}^\chi(v_z^\chi + e\hbar^{-1}B(\boldsymbol{\Omega}_{\mathbf{k}}^\chi \cdot \mathbf{v}_{\mathbf{k}}^\chi))$, $(\tau_{\mathbf{k}}^\chi)^{-1} = \sum_{\mathbf{k}'} W_{\mathbf{k}\mathbf{k}'}^{\chi\chi}$, and $f_{\mathbf{k}}^\chi$ is the new unknown function. The role of chemical potential and the orbital magnetic moment enter $(-\partial g_0/\partial \epsilon_k)$ and a B -dependent energy shift in the dispersion, respectively. Using the Fermi-golden rule and the simplest scenario of point-like non-magnetic disorder, the scattering rate is determined by

$$W_{\mathbf{k}\mathbf{k}'} = \frac{2\pi}{\hbar} |U|^2 \delta(\epsilon_{\mathbf{k}} - \epsilon_{\mathbf{k}'}) \times (1 + \cos\theta \cos\theta' + \sin\theta \sin\theta' \cos(\phi - \phi')). \quad (39)$$

Here, U represents the disorder strength in suitable units. It is crucial to highlight that the explicit dependence on momentum direction, namely the polar and azimuthal angles, arises from the chirality of the Weyl fermion wavefunction. This dependence persists even in the absence of a momentum-dependent disorder strength U . Consequently, the Boltzmann equation simplifies to

$$f^\chi(\theta) = \int F^\chi(\theta') \tau(\theta) (1 + \cos\theta \cos\theta') (f^\chi(\theta') - h^\chi(\theta')) d\theta', \quad (40)$$

where $F^\chi(\theta) = k^3(\theta)(\mathcal{D}_\theta^\chi)^{-1} \sin\theta |\mathbf{v}_{\mathbf{k}} \cdot \mathbf{k}|^{-1}$. All the quantities above are evaluated on the Fermi surface. Incorporating particle conservation by employing the ansatz below solves the aforementioned Boltzmann transport equation.

$$\Lambda^\chi(\theta) = \tau(\theta)(a^\chi + b^\chi \cos\theta - h^\chi(\theta)). \quad (41)$$

Finally, the current is evaluated as:

$$\mathbf{j}^\chi = -e \sum_{\mathbf{k}} \dot{\mathbf{r}}^\chi(g_{\mathbf{k}}^\chi), \quad (42)$$

and thus the longitudinal magnetoconductivity $\sigma_{zz}(B)$ is evaluated. We define $\delta\sigma_{zz}(B) = \sigma_{zz}(B) - \sigma_{zz}^0$, where σ_{zz}^0 is the zero field conductivity.

Figure 8 (a) illustrates the computed Longitudinal

magnetoconductivity coefficient (LMC), $\delta\sigma_{zz}(B)$, for an isolated Weyl node. Remarkably, it consistently exhibits negative LMC, regardless of the Weyl node's chirality. This finding is in sharp contrast to claims from recent studies that suggest that intranode scattering alone could yield positive LMC in Weyl semimetals [49–56]. Figure 8 (b) illustrates $\Lambda^\chi(\theta)$, while Figure 8 (c) displays the normalized distribution function. Notably, the distribution function directly reflects $g_{\mathbf{k}}^\chi$, which integrates to zero, aligning with particle number conservation. Additionally, Ref. [67] also tackles this problem using an ansatz-free numerical solution to the Boltzmann equation yielding consistent results.

2. Single node LMC from Landau levels

Here we briefly review the magnetoconductivity calculation using the Landau level formalism for an isolated single node that is also performed in Ref [67]. The magnetic field is fixed along the z -axis, and the following gauge $\mathbf{A} = (0, Bx, 0)$ is chosen. After Peierls substitution, $\mathbf{k} \rightarrow \boldsymbol{\Pi} = \mathbf{k} + e\mathbf{A}/\hbar$, the following annihilation and creation operators are introduced:

$$\begin{aligned} a &= \frac{l_B}{\sqrt{2}} (\Pi_x - i\Pi_y) \\ a^\dagger &= \frac{l_B}{\sqrt{2}} (\Pi_x + i\Pi_y), \end{aligned} \quad (43)$$

where $l_B = \sqrt{\hbar/eB}$ is the magnetic length. The Hamiltonian for a single Weyl node is rewritten in terms of the new operators as:

$$H = \hbar v_F \begin{pmatrix} k & \frac{\sqrt{2}}{l_B} a \\ \frac{\sqrt{2}}{l_B} a^\dagger & -k \end{pmatrix}, \quad (44)$$

where $k \equiv k_z$, since k_x, k_y are no longer good quantum numbers. The energy spectrum at a single Weyl node is $\epsilon_n(k) = v_F \sqrt{2\hbar n e B} + (\hbar k)^2$, and additionally, there is a zeroth quantum level that is given by $\epsilon_0 = -\chi \hbar v_F k$. The Landau level wavefunctions are given by:

$$|\psi_k\rangle = \frac{1}{\sqrt{\mathcal{N}_k}} \begin{pmatrix} \frac{\sqrt{2(n+1)}}{l_B} \frac{1}{\epsilon_n(k)/\hbar v_F - k} |n\rangle \\ |n+1\rangle \end{pmatrix}, \quad (45)$$

where

$$\mathcal{N}_k = 1 + \frac{2(n+1)}{l_B^2} \frac{1}{(\epsilon_n(k)/\hbar v_F - k)^2}. \quad (46)$$

In Fig. 9, the Landau level spectrum is illustrated at a constant magnetic field strength, varying with k . In subsequent calculations, a fixed electron density (η) is maintained, which is usually the case in experiments. The

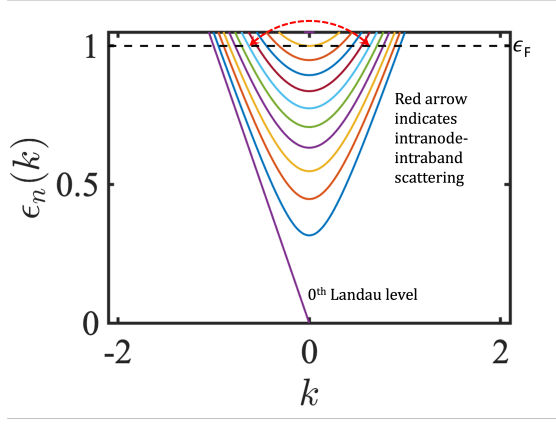


Figure 9. The Landau level spectrum on a single Weyl node. The red arrow indicates the intranode scattering process within the same Landau band (intraband). The zeroth Landau level has no phase space to scatter other than the second node because it is forbidden in the intranode process. Figure adapted from Ref. [67].

expression for η is defined as:

$$\eta = \left(\frac{AeB}{\hbar} \right) \sum_{n=0}^{n_c} \int \rho^n(\epsilon) f^n(\epsilon) d\epsilon, \quad (47)$$

where n represents the Landau level index, n_c denotes the number of occupied Landau levels, $\rho^n(\epsilon)$ characterizes the density of states of the n^{th} band, $f^n(\epsilon)$ denotes its occupancy, and AeB/\hbar is the degeneracy of each level. The expression for the density of states is given by:

$$\rho^n(\epsilon) = \int \frac{dk}{2\pi} \delta(\epsilon - \epsilon_n(k)). \quad (48)$$

$$\rho^{n \geq 1}(\epsilon) = \frac{1}{2\pi\hbar v_F^2} \frac{\epsilon}{\sqrt{\epsilon^2/v_F^2 - 2\hbar n e B}}, \quad (49)$$

$$\rho^0(\epsilon) = \frac{1}{2\pi\hbar v_F}. \quad (50)$$

The electronic density η then becomes

$$\eta = \left(\frac{AeB}{\hbar} \right) \frac{1}{2\pi\hbar} \left[\sum_{n=1}^{n_c} \sqrt{\frac{\epsilon_F^2}{v_F^2} - 2\hbar n e B} + \frac{\epsilon_F}{v_F} \right]. \quad (51)$$

Since the Fermi energy $\epsilon_F = v_F \sqrt{2\hbar n_c e B}$, we have

$$\eta = \left(\frac{AeB}{\hbar} \right) \frac{\sqrt{2\hbar e B}}{2\pi\hbar} \left[\sum_{n=1}^{n_c} \sqrt{n_c - n} + \frac{\epsilon_F}{v_F} \right] \quad (52)$$

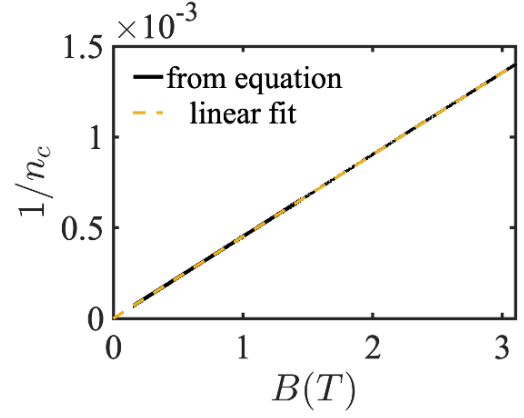


Figure 10. $1/n_c$ as a function of the magnetic field, where n_c is the number of occupied Landau levels. Figure adapted from Ref. [67].

Evaluating the summation above, we find

$$\eta = \left(\frac{AeB}{\hbar} \right) \frac{\sqrt{2\hbar e B}}{2\pi\hbar} \left[-H_z(-1/2, n_c) + Z(-1/2) + \frac{\epsilon_F}{v_F} \right]. \quad (53)$$

Here $H_z(s, x)$ is the Hurwitz-Zeta function and $Z(x)$ is the Riemann-Zeta function. The above equation solves the number for filled Landau levels n_c as a function B . Since the analytical expression for n_c is unavailable, it is calculated numerically by inverting the above equation. In Fig. 10, $1/n_c$ is plotted as a function of the magnetic field that is observed to be perfectly linear in B for a wide range of magnetic fields. The conductivity for each Landau band $n \geq 1$ is given by

$$\sigma^n = \frac{e^2}{\hbar} \int \frac{dk}{2\pi} (v_n^z(k))^2 \tau_k^n \delta(\epsilon_n(k) - \epsilon_F), \quad (54)$$

where

$$v_n^z(k) = \frac{1}{\hbar} \frac{\partial \epsilon_n(k)}{\partial k} = \frac{\hbar k v_F^2}{\epsilon_n(k)}, \quad (55)$$

and τ_k^n is the *intranode, intra-(Landau)-band* scattering time. For point-like non-magnetic impurities this is evaluated as

$$\frac{1}{\tau_k^n} = \frac{n_{\text{imp}} V_{\text{dis}}^2}{\hbar} \int dk' |\langle \psi_k | \psi_{k'} \rangle|^2 \delta(\epsilon_n(k') - \epsilon_F). \quad (56)$$

Here V_{dis} is the disorder strength and n_{imp} is the impurity density.

Before proceeding ahead, it is crucial to highlight the nature of scattering within a single Weyl node and a single Landau band, as depicted in Fig. 9. Specifically, the red arrow's direction illustrates the sole possible scattering channel within a Landau band that conserves energy (elastic scattering). Notably, the zeroth Landau level lacks scattering phase space within the same node,

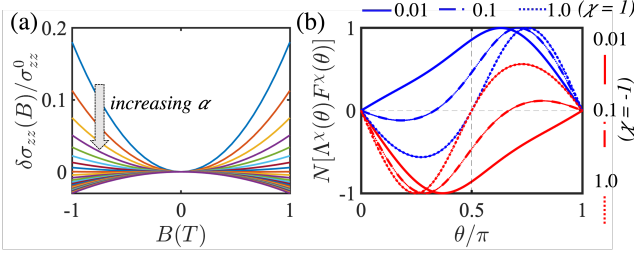


Figure 11. (a) LMC for a pair of Weyl nodes of opposite chiralities becomes negative beyond a critical intervalley scattering strength α_c . Here α is increased from 0.1 to 1. (b) The normalized deviation in distribution functions at both the valleys for three different values of α . Figure adapted from Ref. [67].

$\tau_\phi \gg \tau_{\text{inter}}^c > \tau_{\text{inter}} \text{ (-ve)}$	$\tau_\phi \gg \tau_{\text{inter}} > \tau_{\text{inter}}^c \text{ (+ve)}$
$\tau_{\text{inter}} > \tau_\phi \gg \tau_{\text{intra}} \text{ (-ve)}$	$\tau_{\text{intra}} > \tau_\phi \gg \tau_{\text{inter}} \text{ (-ve)}$

Figure 12. Conditions to observe positive or negative LMC. Figure adapted from Ref. [67].

thereby not contributing to intranode scattering. However, the opposite-chirality Weyl node provides the sole available scattering phase space for the zeroth Landau level (internode scattering). Consequently, we must discount the zeroth Landau level's contribution when calculating the intranode conductivity. The intranode, intra-(Landau)-band scattering time is determined to be

$$\tau_k^n = \frac{\hbar^2 v_F}{n_{\text{imp}} V_{\text{dis}}^2} \frac{\sqrt{\epsilon_F^2 - 2\hbar n e B v_F^2}}{\epsilon_F} \quad (57)$$

The total intranode conductivity is given by

$$\sigma = \sum_{n=1}^{n_c} \sigma^n. \quad (58)$$

Including the degeneracy, we evaluate σ^n to be

$$\sigma^n = \frac{e^2}{2\pi\hbar} \frac{AeB}{\hbar} \frac{\hbar v_F^2}{n_{\text{imp}} V_{\text{dis}}^2} \frac{\epsilon_F^2 - 2\hbar n e B v_F^2}{\epsilon_F^2}. \quad (59)$$

Substituting $\epsilon_F = v_F \sqrt{2\hbar n_c e B}$, and evaluating the summation, we find (all the constant prefactors factors are absorbed in \mathcal{C})

$$\sigma = \mathcal{C} B \sum_{n=1}^{n_c} \left(1 - \frac{n}{n_c}\right) = \mathcal{C} B \left(\frac{n_c - 1}{2}\right) = \frac{\mathcal{C}}{2} (B n_c - B) \quad (60)$$

Since $B n_c$ is a constant (from Fig. 10), we conclude that the intranode conductivity decreases with an increase in the magnetic field.

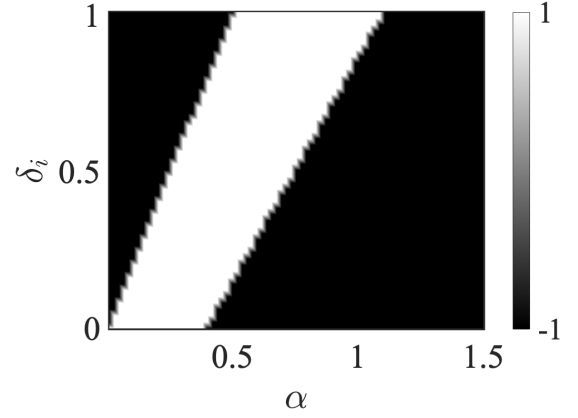


Figure 13. The sign of LMC with the inclusion of inelastic scattering. We choose $V_{\mathbf{k}\mathbf{k}'}^{\chi\chi'} \rightarrow 0$, $V_{\mathbf{k}'\mathbf{k}}^{\chi'\neq\chi} \rightarrow 0$, and thus $\alpha_i = V_{\mathbf{k}'\mathbf{k}}^{\chi\chi}/W_{\mathbf{k}\mathbf{k}'}^{\chi\chi'}$. Figure adapted from Ref. [67].

3. Two-node LMC with internode scattering:

The previous two subsections have established the fact that the longitudinal magnetoresistance from a single Weyl node is negative. Now, returning to the case of a pair of Weyl fermions and the Boltzmann formalism, the collision integral takes the following form

$$\mathcal{I}_{\text{coll}}[f_{\mathbf{k}}^{\chi}] = \sum_{\mathbf{k}'\chi'} \left(\Lambda_{\mathbf{k}}^{\chi} - \Lambda_{\mathbf{k}'}^{\chi'} \right) W_{\mathbf{k}\mathbf{k}'}^{\chi\chi'} (-\partial g_0 / \partial \epsilon_k) eE, \quad (61)$$

where the scattering rate $W_{\mathbf{k}\mathbf{k}'}^{\chi\chi'}$ has both internode and intranode scattering, and is evaluated for non-magnetic pointlike impurities to be:

$$W_{\mathbf{k}\mathbf{k}'}^{\chi\chi'} = \frac{2\pi}{\hbar} |U^{\chi\chi'}|^2 \delta(\epsilon_{\mathbf{k}} - \epsilon_{\mathbf{k}'}) \times (1 + \chi\chi'(\cos\theta\cos\theta' + \sin\theta\sin\theta'\cos(\phi - \phi'))). \quad (62)$$

Here, the disorder parameter $U^{\chi\chi'}$ allows us to control internode and intranode scattering strengths separately. The ratio $|U^{\chi\neq\chi'}|^2 / |U^{\chi=\chi'}|^2 \equiv \alpha$, which is the relative intervalley scattering strength. In Figure 11 (a), we plot LMC against increasing intervalley scattering strength. Remarkably, beyond a critical intervalley scattering strength α_c , the LMC is negative. This trend was reported in Refs. [56, 57, 67], and was attributed to (i) the orbital magnetic moment's opposing effects on the Fermi surfaces of both nodes, and (ii) discarding of the constant relaxation-time approximation.

What is striking here is that even with weak internode scattering, LMC remains positive, contrasting with the scenario of strictly zero internode scattering (previous two subsections). Mathematically, this dissimilarity can be understood as follows: the distribution function obtained under weak internode scattering differs signif-

icantly from that in Fig. 8, where zero internode scattering was assumed. In the latter case, the distribution function's deviation must integrate to zero at a single node to conserve chiral charge. However, this requirement is relaxed in the presence of weak internode scattering, where only global charge conservation is necessary. A more physically transparent interpretation is presented next.

The Boltzmann transport equation provides a steady-state solution applicable when t greatly exceeds the maximum of τ_{inter} and τ_{intra} . Thus, particles are free to scatter and redistribute across both nodes within a timescale much shorter than τ_ϕ . In order to pinpoint the role of τ_ϕ , it is incorporated it into the Boltzmann formalism [67], and it is found that when $\tau_{\text{inter}} \gg \tau_\phi$, one is in an effective one-node regime, and obtains negative LMC, which is fully consistent with the results of a single-node obtained discussed earlier. The role of τ_ϕ is discussed in detail in Sec. III A 4.

These observations underscore several crucial points: (i) intranode scattering alone does not generate positive LMC due to chiral charge conservation, (ii) finite internode scattering is fundamental for observing positive LMC in the semiclassical low- B limit, (iii) positive LMC induced by chiral anomaly is thus an exclusive internode phenomenon, bridging the Boltzmann and Landau-level perspectives, and (iv) surpassing a critical value α_c , sufficiently large internode scattering switches the LMC sign from positive to negative. Consequently, $\tau_\phi \gg \tau_{\text{inter}} > \tau_{\text{inter}}^c$ becomes imperative in experimental settings to observe positive LMC, where τ_{inter}^c represents the critical intervalley scattering time below which LMC turns negative. Fig. 12 summarizes the conditions.

4. Inclusion of inelastic scattering

The discussion so far result in the following conundrum. Note that (i) LMC is negative when $\alpha = 0$, (ii) LMC is positive when $\alpha > 0$, (iii) LMC is negative when $\alpha > \alpha_c$. How does an infinitesimal intervalley scattering suddenly switch the sign of LMC? The inclusion of τ_ϕ , which is an inelastic scattering timescale, is imperative to resolve this issue and was presented in Ref. [67]. We briefly review this here.

For elastic scattering, the scattering rate from state $|\mathbf{k}\rangle$ to $|\mathbf{k}'\rangle$ is identical to the rate from $|\mathbf{k}'\rangle$ to $|\mathbf{k}\rangle$. In other words, we can express the collision integral as:

$$\mathcal{I}_{\text{coll}}[g_{\mathbf{k}}^x] = \sum_{\chi'} \sum_{\mathbf{k}'} \left(g_{\mathbf{k}'}^{\chi'} - g_{\mathbf{k}}^x \right) W_{\mathbf{k}\mathbf{k}'}^{\chi\chi'}. \quad (63)$$

We'll introduce another scattering rate, denoted as $V_{\mathbf{k}\mathbf{k}'}^{\chi\chi'}$, to encompass inelastic scattering within the medium. It follows that $V_{\mathbf{k}\mathbf{k}'}^{\chi\chi'} \neq V_{\mathbf{k}'\mathbf{k}}^{\chi\chi'}$, enabling us to express the

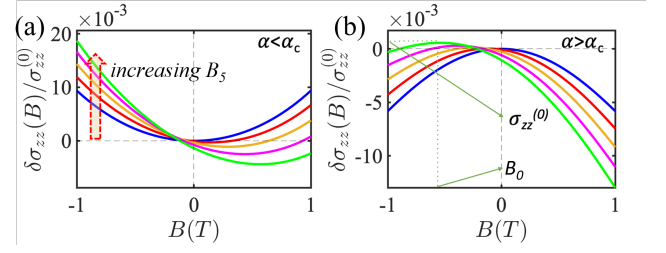


Figure 14. LMC v/s \mathbf{B} at different values of \mathbf{B}_5 for the cases when intervalley scattering is less and greater than some critical value α_c . For $\alpha < \alpha_c$ the effect of \mathbf{B}_5 field results in tilt and shift of the LMC parabola, which is dubbed as the weak sign reversal, while for the case $\alpha > \alpha_c$ the LMC parabola is reversed, tilted and shifted, thus dubbed as *strong* and *weak* sign reversal. Figure adapted from Ref. [69].

total collision integral as:

$$\begin{aligned} \mathcal{I}_{\text{coll}}[g_{\mathbf{k}}^x] = & \sum_{\chi'} \sum_{\mathbf{k}'} \left(g_{\mathbf{k}'}^{\chi'} - g_{\mathbf{k}}^x \right) W_{\mathbf{k}\mathbf{k}'}^{\chi\chi'} \\ & + \sum_{\chi'} \sum_{\mathbf{k}'} \left(V_{\mathbf{k}'\mathbf{k}}^{\chi'\chi} g_{\mathbf{k}'}^{\chi'} - V_{\mathbf{k}\mathbf{k}'}^{\chi\chi'} g_{\mathbf{k}}^x \right). \end{aligned} \quad (64)$$

Substituting the ansatz for $g_{\mathbf{k}}^x$, the Boltzmann equation becomes

$$\begin{aligned} \mathcal{D}^x \left[v_z^x + \frac{eB}{\hbar} (\boldsymbol{\Omega}^x \cdot \mathbf{v}_{\mathbf{k}}^x) \right] = & \sum_{\chi'} \sum_{\mathbf{k}'} W_{\mathbf{k}\mathbf{k}'}^{\chi\chi'} (\Lambda_{\mathbf{k}'}^{\chi'} - \Lambda_{\mathbf{k}}^x) \\ & + \sum_{\chi'} \sum_{\mathbf{k}'} (V_{\mathbf{k}'\mathbf{k}}^{\chi'\chi} \Lambda_{\mathbf{k}'}^{\chi'} - V_{\mathbf{k}\mathbf{k}'}^{\chi\chi'} \Lambda_{\mathbf{k}}^x). \end{aligned} \quad (65)$$

The modified valley scattering rate is:

$$\frac{1}{\tau_{\mathbf{k}}^x} = \nu \sum_{\chi'} \int \frac{d^3\mathbf{k}'}{(2\pi)^3} (\mathcal{D}_{\mathbf{k}'}^{\chi'})^{-1} \left(W_{\mathbf{k}\mathbf{k}'}^{\chi\chi'} + V_{\mathbf{k}\mathbf{k}'}^{\chi\chi'} \right), \quad (66)$$

and the Boltzmann equation becomes:

$$\begin{aligned} \mathcal{D}^x \left[v_z^x + \frac{eB}{\hbar} (\boldsymbol{\Omega}^x \cdot \mathbf{v}_{\mathbf{k}}^x) \right] + \frac{\Lambda_{\mathbf{k}}^x}{\tau_{\mathbf{k}}^x} = & \sum_{\chi'} \sum_{\mathbf{k}'} (W_{\mathbf{k}'\mathbf{k}}^{\chi'\chi} + V_{\mathbf{k}'\mathbf{k}}^{\chi'\chi}) \Lambda_{\mathbf{k}'}^{\chi'}. \end{aligned} \quad (67)$$

To account for the impact of inelastic scattering on the valley scattering time, we can make the following substitution: $W_{\mathbf{k}\mathbf{k}'}^{\chi\chi'} \rightarrow -V_{\mathbf{k}\mathbf{k}'}^{\chi\chi'} + W_{\mathbf{k}\mathbf{k}'}^{\chi\chi'}$. With this modification, the valley scattering time maintains its original expression, while the Boltzmann equation transforms to:

$$\mathcal{D}^x \left[v_z^x + \frac{eB}{\hbar} (\boldsymbol{\Omega}^x \cdot \mathbf{v}_{\mathbf{k}}^x) \right] + \frac{\Lambda_{\mathbf{k}}^x}{\tau_{\mathbf{k}}^x} = \sum_{\chi'} \sum_{\mathbf{k}'} W_{\mathbf{k}'\mathbf{k}}^{\chi'\chi} (1 + \delta_i) \Lambda_{\mathbf{k}'}^{\chi'}, \quad (68)$$

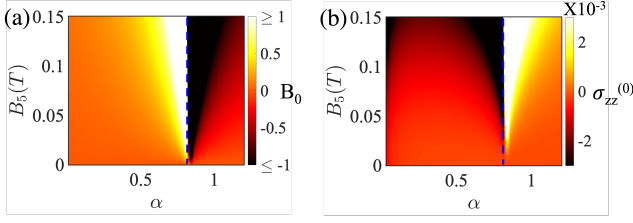


Figure 15. (a) The vertex of the parabola B_0 , and (b) conductivity at B_0 for a minimal model of untilted TR broken WSM. Around the blue dashed contour ($\alpha = \alpha_c$) we see a ‘strong’ sign-reversal. The parameters B_0 and $\sigma_{zz}^{(0)}$ show a striking change of sign as we move across the α_c contour. Figure adapted from Ref. [69].

where

$$\delta_i = \frac{-V_{\mathbf{k}\mathbf{k}'}^{\chi\chi'} + V_{\mathbf{k}'\mathbf{k}}^{\chi'\chi}}{W_{\mathbf{k}\mathbf{k}'}^{\chi\chi'}}. \quad (69)$$

When $\delta_i = 0$, the scenario corresponds to elastic scattering. Figure 13 illustrates the sign of longitudinal magnetoconductance as a function of both the inelastic scattering coefficient δ_i and the intervalley scattering strength α , both normalized with respect to the intravalley scattering strength. First, considering the limit as $\delta_i \rightarrow 0$, implying τ_ϕ as the largest timescale in the system. With τ_{inter} large but still less than τ_ϕ (i.e., when $\alpha \ll 1$), positive LMC is observed. Decreasing τ_{inter} (increasing α) leads to an inversion from positive to negative LMC at a critical value of intervalley scattering strength α_c , consistent with previous discussion. Next, exploring scenarios with large but finite τ_ϕ (i.e., $0 < \delta_i < 1$), we find that if α is smaller than $f\delta_i$, where f represents a fraction less than one (i.e., when $\tau_\phi < f\tau_{\text{inter}}$), one operates within the effective one-node regime, yielding negative LMC consistent with single-node results. The value of f , however, is non-universal and relies on microscopic parameters, with $f = 1/2$ observed here. Furthermore, by maintaining δ_i fixed, increasing α (i.e., decreasing τ_{inter}) results in an inversion of LMC sign at some critical value of the intervalley scattering strength.

B. Magnetotransport in inhomogeneous Weyl semimetals

Having discussed the nature of longitudinal magnetoconductance in weakly disordered Weyl semimetals, we now move to the discussion of magnetotransport in inhomogeneous WSMs and illustrate the effects of strain on magnetotransport. Recent studies [80, 113–118] have investigated the effect of elastic deformations (or strain) on massless Dirac fermions. Strain is shown to couple as an axial magnetic field (also termed a chiral gauge field) to Dirac/Weyl fermions. In graphene, for instance, spectroscopic measurements of Landau levels reveal strain-

induced fields reaching up to 300T [118]. In Weyl semimetals, strain has been shown to produce adjustable variations in carrier mobility, electronic conductivity, and even phase transitions [115, 119–135]. The complex interactions between strain, electronic structure, and transport behavior are highlighted by several theoretical models and simulations, which shed light on the underlying mechanisms driving these phenomena [69, 124, 136–138].

In a minimal model of time-reversal symmetry broken Weyl semimetal, Weyl nodes are separated in momentum space by a vector \mathbf{b} such that topological protection is ensured. The vector \mathbf{b} is also interpreted as an axial gauge field and it couples with an opposite sign to Weyl nodes of opposite chirality [46, 139–142]. Spatially varying \mathbf{b} thus generates an axial magnetic field $\mathbf{B}_5 = \nabla \times \mathbf{b}$, which also couples oppositely to Weyl nodes of opposite chirality. An effective \mathbf{B}_5 field thus emerges from an inhomogeneous strain profile in Weyl semimetals. In the presence of this effective chiral gauge field \mathbf{B}_5 , the effective magnetic field experienced by Weyl fermions at a given node of chirality χ is $\mathbf{B} \rightarrow \mathbf{B} + \chi\mathbf{B}_5$. In a recent work Grushin *et al.* [80] have pointed out that even in the absence of an external magnetic field, the chiral gauge field influences the diffusive electron transport in Weyl semimetals by modifying its longitudinal magnetoconductance. Specifically, they show that strain, alone, results in positive LMC even in the absence of an external magnetic field. However, recent works, which consider momentum-dependent scattering beyond the relaxation-time approximation find contrary results [67, 69]. On similar lines, Ghosh *et al.* [143] point out that the planar Hall conductance can be manipulated by strain as well. However, contrary to this finding, refs. [67, 69] conclude that the strain-induced contribution is not only opposite to that of the regular planar Hall effect but is also different in magnitude. We briefly review these findings below.

Strain-induced magnetotransport can be studied using the semiclassical approximation discussed before by considering a valley-dependent magnetic field. First, we assume that \mathbf{B}_5 is held parallel to the electric \mathbf{E} and the external magnetic field, \mathbf{B} , and calculate σ_{zz} . The behavior of $\delta\sigma_{zz}(B)$, or the change in LMC caused by the magnetic field, is plotted in Fig. 14. This change in conductance can be expressed as follows: $\delta\sigma_{zz}(B) = \sigma_{zz}(B) - \sigma_{zz}(B = 0)$. We see that the direction of the magnetic field, particularly near $B = 0$, affects whether and how much LMC increases or decreases. The conductance increases for a negative magnetic field and decreases for a positive magnetic field. Moreover, the conductance increases (decreases) for both positive and negative values of B when $\alpha < \alpha_c$ ($\alpha > \alpha_c$), when the magnitude of B is increased further away from zero. We may compare this to the non-strained behavior, where the behavior of conductance depends on the strength of the magnetic field and either increases (when $\alpha < \alpha_c$) or decreases (when $\alpha > \alpha_c$) as seen in Fig. 11.

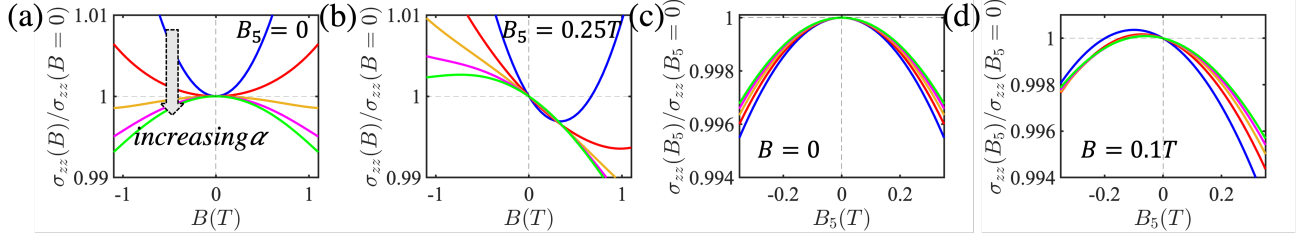


Figure 16. Longitudinal magnetoconductivity for a minimal model of TR broken untitled Weyl semimetal. (a) Increasing intervalley scattering strength results in strong sign reversal. (b) In addition to this, infinitesimal strain now results in weak sign-reversal as well. (c) When plotted as a function of the gauge field B_5 , LMC is always strongly sign-reversed. (d) In the presence of an external magnetic field, we see signatures of weak-sign reversal as well. In all the plots as we move from blue to the green curve we increase the intervalley scattering strength α from below α_c to above α_c . Figure adapted from Ref. [69].

In pursuit of clarifying the intricacies in magnetoconductivity behavior discussed above, Ahmad *et al.* [69] begin by generalizing the magnetoconductivity expression as:

$$\sigma_{zz}(B) = \sigma_{zz}^{(2)} + \sigma_{zz}^{(0)} + (B - B_0)^2. \quad (70)$$

To align with the observations depicted in Fig. 14, the vertex of the parabola (B_0) is adjusted further from the origin utilizing the aforementioned definition. Consequently, while LMC is consistently positive around the vertex B_0 in Fig. 14(a) when the strength of the intervalley scattering $\alpha < \alpha_c$, it is negative at small values of positive magnetic fields. In essence, LMC remains positive when considering the change in magnetic field and conductivity about the conductivity at B_0 , rather than about the origin. The authors of Ref. [69] term this as *weak* sign-reversal, as this phenomenon arises due to the preserved orientation of the parabola with only the vertex relocated away from the origin, and importantly $\sigma_{zz}^{(2)}$ retains its positive sign. Thus, strain in inhomogeneous Weyl semimetals induces the system into a state of “*weak*” sign-reversal along a specific direction of the magnetic field when intervalley scattering is weak. Summarily, the features characterizing weak sign-reversal include (i) $B_0 \neq 0$, (ii) $\sigma_{zz}^{(0)} \neq \sigma_{zz}(B=0)$, and (iii) $\text{sign } \sigma_{zz}^{(2)} > 0$.

Conversely, in Fig. 14(b), the orientation of the parabola is inverted upon surpassing the critical threshold of intervalley scattering strength (α_c). Consequently, $\sigma_{zz}^{(2)}$ becomes negative, resulting in a decrease of LMC relative to B_0 . This phenomenon is termed “*strong*” sign-reversal [69]. Unlike its weak counterpart, strong sign-reversal lacks restrictions on the values of B_0 and $\sigma_{zz}^{(0)}$, being solely governed by the condition: (i) $\text{sign } \sigma_{zz}^{(2)} < 0$. In conclusion, the distinctive features of both “*strong and weak*” sign-reversal are: (i) $B_0 \neq 0$, (ii) $\sigma_{zz}^{(0)} \neq \sigma_{zz}(B=0)$, and (iii) $\text{sign } \sigma_{zz}^{(2)} < 0$.

In Fig. 15, we show how the parameters B_0 and $\sigma_{zz}^{(0)}$ depend on the chiral gauge field and intervalley scattering strength. The transition between the ‘weak’ and ‘strong and weak’ cases (and vice versa) is characterized by an

abrupt reversal in the signs of the relative offset in conductivity $\sigma_{zz}^{(0)}$, alongside the vertex of the parabola B_0 , where $B_0 \leq 0$ when $\sigma_{zz}^{(0)} \geq 0$, and vice versa. However, $\sigma_{zz}^{(2)}$ exhibits continuous interpolation across zero (not depicted in the plot). Notably, no discontinuity in B_0 or $\sigma_{zz}^{(0)}$ is observed in the weak sign-reversed case. In other words, as the strain-induced field increases from zero for a constant intervalley scattering, the parameters B_0 and $\sigma_{zz}^{(0)}$ undergo continuous variation.

In Fig. 16, the longitudinal magnetoconductivity is plotted as a function of magnetic field for various values of intervalley scattering. In the absence of a chiral gauge field (Fig. 16(a)), as anticipated, we discern strong sign-reversal when $\alpha > \alpha_c$. However, in the presence of a chiral gauge field (Fig. 16(b)), we observe both strong and weak sign-reversal phenomena, as discussed before. In Fig. 16(c), the longitudinal magnetoconductance is plotted exclusively as a function of the chiral gauge magnetic field (i.e., $B = 0$). With no external magnetic field present in this scenario, the delineation of positive/negative LMC and weak/strong sign-reversal is solely being defined with respect to the B_5 field. It is seen that strain-induced chiral gauge field alone consistently yields a strong sign-reversed phase, irrespective of the intervalley scattering strength! Notably, this observation holds even in the presence of an external B -field (Fig. 16(d)). Interestingly, earlier studies suggest that strain alone can lead to a positive contribution to the longitudinal magnetoconductance (LMC) even in the absence of an external magnetic field ($\mathbf{B} = 0$) [80]. However, Fig. 16 reveals a striking contrast: strain alone results in a decrease in conductance. In the absence of strain, the transition of LMC from positive to negative is also attributed to the effect of the orbital magnetic moment (OMM). However, even when disregarding the contribution of OMM, the results shown in Fig. 16 remain qualitatively unchanged. This is because, unlike in the former scenario, strain-induced OMM impacts both nodes equally, thereby preserving the similarity of the Fermi surfaces.

C. Planar Hall effect

We now discuss another aspect of the chiral anomaly, specifically the planar Hall effect (PHE) [64, 144]. This effect occurs when there is an in-plane transverse voltage due to the misalignment of coplanar electric and magnetic fields. The planar Hall conductivity (PHC), denoted as σ_{zx} , measures the transverse conductivity along the \hat{z} direction, perpendicular to both the applied electric field and the current in the \hat{z} direction, and under the influence of a magnetic field in the x - z plane that makes an angle γ with respect to the x -axis (see Fig. 6). This phenomenon is well-known in ferromagnetic systems [145–149], showing an angular dependence similar to that observed in Weyl semimetals (WSMs). In Ref. [64], Nandy *et al.* developed a semiclassical transport theory of the PHE linking it to the occurrence of chiral anomaly and Berry curvature. Subsequent works [66, 150–159] have studied PHE and its corresponding thermal transport responses in the context of Weyl, Dirac and spin-orbit coupled metals, using it as another probe of the chiral anomaly in these materials. The crucial role of internode scattering in the planar Hall effect considering momentum-dependent scattering and charge conservation was studied in Ref. [57] where it was concluded that unlike LMC, the planar Hall conductivity does not switch sign for any value of the internode scattering strength. Furthermore, the behavior with respect to the external magnetic field is quadratic, and the dependence on the orientation of the magnetic field is $\sin(2\gamma)$ irrespective of the strength of intervalley scattering.

Similar to LMC, the dependence on the magnetic field is typically quadratic and we may expand the planar Hall conductivity σ_{xz} as

$$\sigma_{xz}(B) = \sigma_{xz}^{(2)}(B - B_0)^2 + \sigma_{xz}^{(0)}, \quad (71)$$

where B_0 is vertex of the parabola, and $\sigma_{xz}^{(2)}$ is the quadratic coefficient. To discuss the effect of strain, we begin by evaluating the planar Hall conductivity in the absence of an external magnetic field [69]. Fig. 17 presents the planar Hall conductivity $\sigma_{xz}(B_5)$, computed without an external magnetic field. The angular dependence on γ_5 follows the relation $\sim \sin(2\gamma_5)$, consistent with the behavior observed in conventional planar Hall conductivity [69]. Additionally, Ahmad *et al.* examined the impact of intervalley scattering [69], and their numerical analysis reveals that the planar Hall conductivity induced by the chiral gauge field behaves as $\sim 1/\alpha$.

In Ref. [69], the authors investigate the behavior of the planar Hall conductivity under two distinct conditions: (a) when an external magnetic field is applied and the strain-induced field is absent, and (b) when the strain-induced field is present and the external magnetic field was absent. It is found that the contributions to the planar Hall conductivity differ both in sign and magnitude, contrasting earlier claims [143]. Specifically, $\sigma_{xz}(B)$ increases with increasing B , while $\sigma_{xz}(B_5)$ decreases with

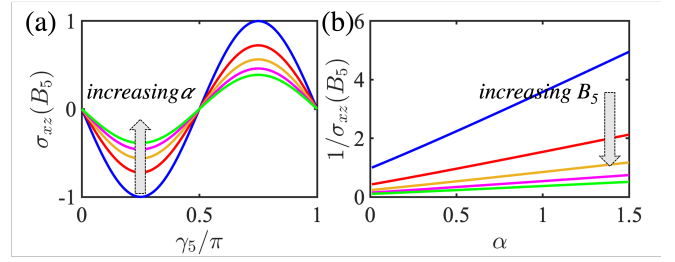


Figure 17. Planar Hall conductivity for a minimal model of untitled TR broken WSM in the absence of any magnetic field. (a) Variation with respect to the angle γ_5 . Increasing α reduces the conductivity. (b) PHC behaves as the inverse of scattering strength. Since $\sigma_{xz}(B_5 = 0) = 0$, we have normalized σ_{xz} appropriately in both the plots. Increasing the B_5 field increases the conductivity. Figure adapted from Ref. [69].

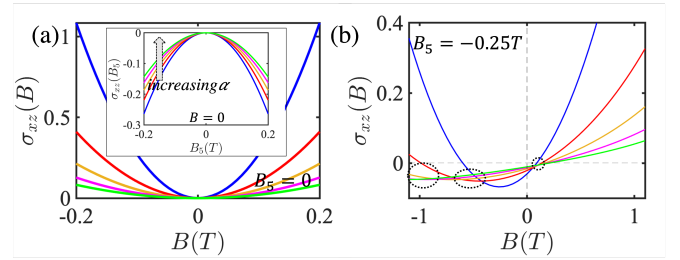


Figure 18. Planar Hall conductivity for a minimal model of untitled TR broken WSM. (a) PHC as a function of the external magnetic field B and no strain-induced field ($B_5 = 0$). Inset: PHC has been plotted as a function of B_5 with no external field ($B = 0$). The angle γ was chosen to be equal to γ_5 . (b) PHC in the presence of both magnetic field and strain. The chiral gauge field causes weak sign-reversal. The dotted ellipses highlight regions that show an anomalous behavior with respect to intervalley scattering strength. All the plots are appropriately normalized. Figure adapted from Ref. [69].

increasing B_5 . This feature is illustrated in Fig. 18 (a). In other words, the chiral gauge field alone results in a strong sign-reversal. This has been attributed to the inclusion of intervalley scattering, momentum dependence, and charge conservation, which were neglected in previous studies.

When both external magnetic field and chiral gauge fields are present, the strain effect shifts and tilts the conductivity parabola, leading to a weak sign-reversal of the conductivity, as illustrated in Fig. 18(b). Unlike longitudinal magnetoconductivity, the planar Hall conductivity (PHC) does not exhibit a strong sign-reversal, even when the intervalley scattering exceeds the critical value. Interestingly, within a specific window of the magnetic field, increasing the intervalley scattering strength enhances the magnitude of the planar Hall conductivity, which seems counter-intuitive. This behavior can be understood by considering the opposing effects of strain-induced PHC and magnetic field-induced PHC, each contributing oppositely and unequally to the overall planar

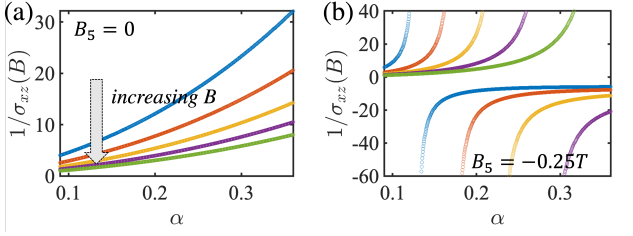


Figure 19. Planar Hall conductance for a minimal model of untilted WSM as a function of intervalley scattering strength. (a) in absence of B_5 field. (b) in presence of B_5 field. In all the curves, as we go from blue to green, we increase B . All the plots are appropriately normalized. Figure adapted from Ref. [69].

Hall conductivity [69]. This phenomenon is more clearly visualized in Fig. 19, where the planar Hall conductivity is plotted as a function of the intervalley scattering strength α . In the absence of a B_5 field, the Hall conductivity is non-linear as a function of $1/\alpha$, which is in contrast to Fig. 17(b) (where $B = 0$, $B_5 \neq 0$), which exhibits linear behavior across all ranges of α . Furthermore, in the presence of a B_5 field, the behavior of σ_{xz} with respect to α can be markedly different. Due to the weak sign-reversal, σ_{xz} can switch its sign, explaining the divergences observed in Fig. 19(b). Additionally, when σ_{xz} transitions from positive to negative, its dependence on α becomes anomalous; specifically, increasing α increases the magnitude of σ_{xz} . Such an anomalous behavior with respect to the intervalley scattering strength is not observed in longitudinal magnetoconductivity.

D. Inversion asymmetric WSM

Having discussed the model of a simple time-reversal symmetry broken Weyl semimetal, here we review inversion asymmetric WSMs. Following Ref. [69], we focus on a minimal model for an inversion asymmetric WSM consisting of four nodes. The Hamiltonian for this system is given by:

$$H = \sum_{n=1}^4 (\chi_n \hbar v_F \mathbf{k} \cdot \boldsymbol{\sigma} + \hbar v_F t_z^n k_z \sigma_0), \quad (72)$$

where the system comprises four Weyl nodes located at $\mathbf{K} = (\pm k_0, 0, \pm k_0)$ in the Brillouin zone. In Eq. (72), χ_n denotes the chirality, and t_z^n represents the tilting of the Weyl cone, which is assumed to be along the z direction. Specifically, we have:

$$(1, t_z) = (\chi_1, t_z^{(1)}) = (-\chi_2, t_z^{(2)}) \quad (73)$$

$$= (\chi_3, -t_z^{(3)}) = (-\chi_4, -t_z^{(4)}), \quad (74)$$

such that inversion symmetry is broken. The tilt parameter t_z is considered to be less than unity. Fig. 20(a)

illustrates this prototype inversion asymmetric Weyl semimetal. There are four intranode scattering channels (node $n \leftrightarrow n$) and four internode scattering channels (node $n \leftrightarrow [n+1] \bmod 4$). The dimensionless scattering strength between nodes m and n is denoted as α^{mn} . For simplicity, scattering between nodes $(4 \leftrightarrow 2)$ and $(1 \leftrightarrow 3)$ is ignored. The internode scatterings are categorized as follows:

1. Scattering between Weyl cones of opposite chirality and opposite tilt orientation ($1 \leftrightarrow 2$ and $3 \leftrightarrow 4$).
2. Scattering between Weyl cones of opposite chirality and same tilt orientation ($1 \leftrightarrow 4$ and $2 \leftrightarrow 3$).

These two categories exhibit different behaviors, and uncovering their interplay is of particular interest.

We first explore the behavior of longitudinal magnetoconductivity in the absence of strain. Previously, it was established that for a system with two tilted cones of opposite chirality, ‘weak’ sign-reversal is possible only if the cones are oppositely oriented. In the current scenario, however, the ‘weak’ sign-reversal produced by the internode scattering channel ($1 \iff 2$) is exactly offset by the scattering channel ($4 \iff 3$). Furthermore, the scattering channels ($1 \iff 4$) and ($2 \iff 3$) do not induce weak sign-reversal because they involve Weyl cones with the same tilt. Thus, in the absence of a B_5 field, weak sign-reversal is not observed in the case of an inversion asymmetric WSM.

In Fig. 20, the longitudinal magnetoconductivity for the inversion asymmetric Weyl semimetal described by Eq. 72 is plotted without the strain-induced chiral gauge field B_5 . As discussed, no weak sign-reversal is observed; only strong sign-reversal occurs when α_{12} and/or α_{14} are sufficiently large. Increasing the tilt does not qualitatively alter this behavior; rather, an increase in the magnitude of the tilt in either direction only enhances the magnetoconductivity.

Next, we review the behavior in the absence of an external magnetic field but in the presence of a strain-induced gauge field B_5 . Similar to time-reversal broken Weyl semimetals, the strain-induced chiral magnetic field B_5 results in a negative longitudinal magnetoconductivity (LMC) coefficient $\sigma_{zz}^{(2)}$. This finding contradicts previous claims that strain increases longitudinal magnetoconductivity [141, 143]. The contradiction arises due to the omission of intervalley scattering, momentum-dependent scattering, and charge conservation in these earlier studies, which are all considered in Ref. [69]. Furthermore, it is revealed that strain alone induces strong sign-reversal, while the presence of tilt additionally causes weak sign-reversal. Fig. 21(a) illustrates LMC as a function of the strain-induced magnetic field B_5 , showcasing these features. The magnetoconductivity is modeled by the following expression:

$$\sigma_{zz}(B_5) = \sigma_{zz}^{(2)}(B - B_{50})^2 + \sigma_{zz}(B_{50}). \quad (75)$$

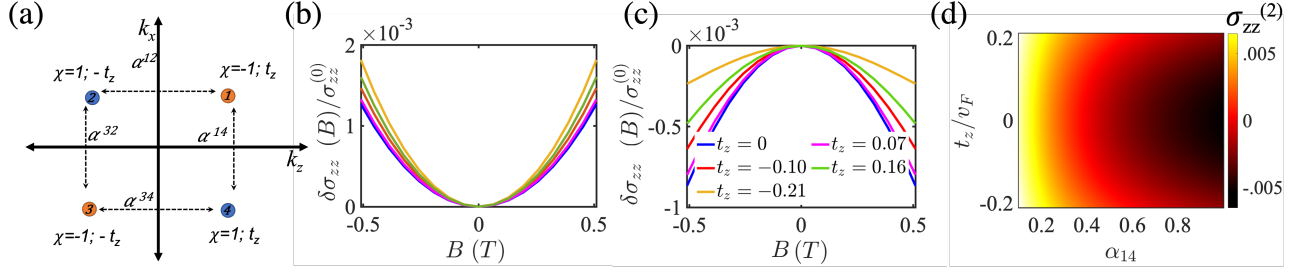


Figure 20. (a) Schematic of Weyl nodes in a prototype model of an inversion asymmetric Weyl semimetal. Here χ is the chirality, t_z is the tilt, and α^{ij} are scattering rates from node i to node j . (b) LMC as a function of magnetic field when the intervalley scattering rates are less than the critical value. (c) LMC as a function of magnetic field when the intervalley scattering rates are above the critical value. The legends in (b) and (c) are identical. (d) $\sigma_{zz}^{(2)}$ for a fixed value of $\alpha_{12} = 0.19$. Plots (b), (c), and (d) are in the absence of strain, i.e., $B_5 = 0$. Figure adapted from Ref. [69].

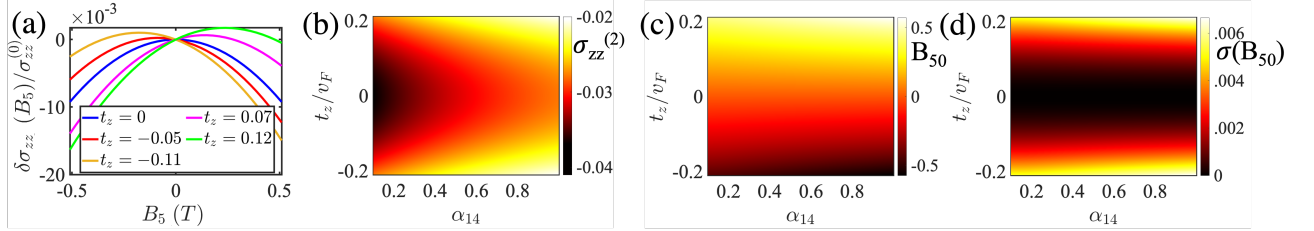


Figure 21. LMC for inversion asymmetric Weyl semimetal in the presence of strain induced chiral magnetic field (B_5) and absence of magnetic field. (a) A finite tilt can result in weak sign-reversal. The plot is for a fixed value of $\alpha_{12} = 0.4$, but the qualitative behavior is independent of scattering strength. (b), (c), and (d) plot the parameters $\sigma_{zz}^{(2)}$, B_{50} , and $\sigma(B_{50})$ as a function of parameters α_{14} and t_z . We fixed $\alpha_{12} = 0.19$. Figure adapted from Ref. [69].

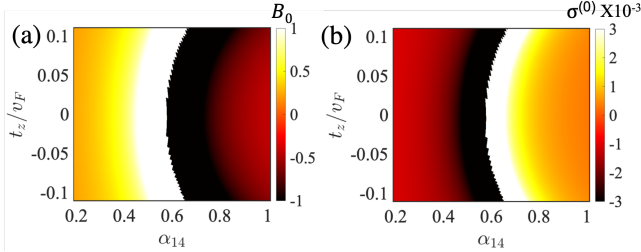


Figure 22. The parameters B_0 (a) and $\sigma^{(0)}$ (b) for inversion asymmetric Weyl semimetals (Eq. 72) in the presence of both strain-induced field and external magnetic field. We have fixed $\alpha_{12} = 0.3$, $B_5 = 0.1T$. Weak sign reversal is not observed and strong sign-reversal occurs at $\alpha_{14} = \alpha_{14c}(t_z)$. Figure adapted from Ref. [69].

The slope $\sigma_{zz}^{(2)}$ is consistently negative, irrespective of tilt, strain, or intervalley scattering strengths across the nodes. The parabola's center, B_{50} , correlates directly with the tilt parameter t_z . The sign of t_z determines whether B_{50} is positive or negative. Although B_{50} also depends on the scattering strength, this dependence is weaker compared to its dependence on t_z . Fig. 21(b), (c), and (d) plot the parameters $\sigma_{zz}^{(2)}$, B_{50} , and $\sigma_{zz}(B_{50})$ as functions of α_{14} and t_z , while keeping α_{12} fixed and $B = 0$. No sharp discontinuities are observed in these

parameters since there is already a strongly sign-reversed state.

In inversion asymmetric inhomogeneous Weyl semimetals, the interplay between the strain-induced chiral gauge field, external magnetic field, and the tilt parameter produces intriguing effects, as demonstrated in Fig. 22. The longitudinal magnetoconductivity (LMC) is analyzed as a function of the external magnetic field for a fixed chiral gauge field. Eq. 70 is used to determine the fit parameters B_0 , $\sigma_{zz}^{(2)}$, and $\sigma_{zz}^{(0)}$. These results show that weak sign-reversal is absent. Instead, strong sign-reversal appears when the intervalley scattering parameter α_{14} exceeds a critical value α_{14c} , which depends on the tilt parameter. Near the critical value $\alpha_{14c}(t_z)$, there is a pronounced shift in the signs of the parameters B_0 and $\sigma_{zz}^{(0)}$, indicating a continuous change in the sign of $\sigma_{zz}^{(2)}$. This behavior highlights the complex interaction between strain, magnetic field, and tilt in these materials. Identifying the parameters B_0 and $\sigma_{zz}^{(0)}$ from experimentally measured conductivity can reveal the dominant scattering mechanisms in the system, such as internode or intranode scattering. These parameters also provide insights into the strain present in the samples and the tilting of the Weyl cones. Experimentally, LMC in inversion asymmetric Weyl semimetals can be explored by adjusting the strain in the system, making it crucial to study the effects of varying strain on LMC.

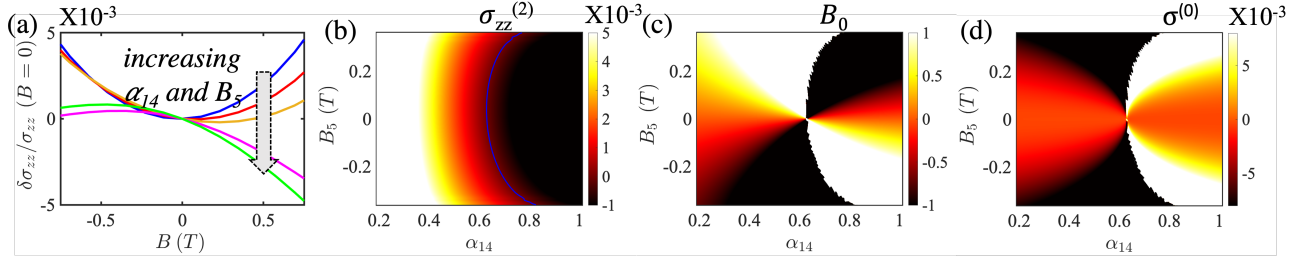


Figure 23. (a) LMC for inversion asymmetric Weyl semimetal. As we move from the blue to the green curve, we simultaneously increase B_5 as well as α_{14} . Both weak and strong sign-reversal are exhibited. The plots (b), (c), and (d) plot the parameters $\delta\sigma_{zz}^{(2)}$, B_0 , and $\sigma^{(0)}$ for fixed α_{12} and $t_z \neq 0$. The blue contour in plot (b) separates the phases where $\sigma_{zz}^{(2)}$ changes sign. Again, we see signatures of both weak and strong sign-reversal. The tilt parameter is fixed to $t_z/v_F = -0.1$. Figure adapted from Ref. [69].

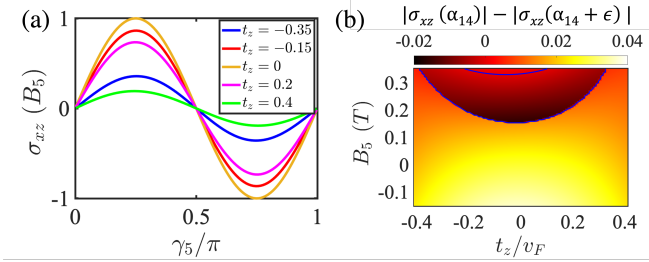


Figure 24. Planar Hall conductance for inversion asymmetric Weyl semimetal. (a) PHC as a function of γ_5 , when $B = 0$, and $B_5 \neq 0$. (b) The change in the magnitude of the planar Hall conductivity on increasing α_{14} infinitesimally. In the region between the blue contours, we observe an anomalous increase in conductivity. Here we fix, $B = 1T$, $\alpha_{12} = 0.4$, $\alpha_{14} = 0.5$, and $\epsilon = 0.01$. Figure adapted from Ref. [69].

Fig. 23(a) shows $\delta\sigma_{zz} = \sigma_{zz}(B) - \sigma_{zz}(B = 0)$ as both the intervalley scattering strength α_{14} and the strain-induced chiral gauge field B_5 are varied. The plot reveals the presence of both weak and strong sign-reversal effects. When α_{14} exceeds the critical value α_{14c} , strong sign-reversal occurs, while variations in the tilt parameter lead to weak sign-reversal. By keeping α_{12} fixed, we can fit the parameters of $\sigma_{zz}(B)$ using Eq. 70. Fig. 23(b) displays $\sigma_{zz}^{(2)}$ as a function of B_5 and α_{14} . The critical contour α_{14c} , where $\sigma_{zz}^{(2)}$ changes sign, is influenced by B_5 , indicating that α_c is generally a function of both the tilt parameter t_z and B_5 . Figs. 23(c) and (d) plot B_0 and $\sigma_{zz}^{(0)}$, respectively, derived from Eq. 70. These plots exhibit interesting behavior as B_5 and α_{14} are varied. In Fig. 23(c), when $\alpha < \alpha_c(B_5)$, B_0 shifts from negative to positive as B_5 transitions from negative to positive. When $\alpha > \alpha_c(B_5)$, B_0 changes from positive to negative. At the critical point $\alpha = \alpha_c(B_5)$, there is a pronounced sign-reversal, creating sharp contrasts on either side of $\alpha_c(B_5)$. In Fig. 23(d), $\sigma_{zz}^{(0)}$ does not change sign with variations in B_5 , but it shows significant behavior around $\alpha_c(B_5)$ due to strong sign-reversal, similar to B_0 . This behavior underscores the complex interplay

between strain, scattering, and tilt in influencing LMC in these materials.

We also review the planar Hall effect in inversion asymmetric Weyl semimetals. Fig. 24(a) presents the planar Hall conductivity (PHC) σ_{xz} as a function of the angle γ_5 when there is no external magnetic field but a strain-induced gauge field B_5 is present. The PHC follows a $\sim \sin(2\gamma_5)$ pattern. This occurs because the contributions from pairs of Weyl nodes that are time-reversed and have opposite tilts add together, while the contributions from pairs of Weyl nodes that are time-reversed and have the same tilt cancel out. This cancellation is why we do not observe a $\sim \sin(\gamma_5)$ trend. In Fig. 24(b), we plot the change in the magnitude of the planar Hall conductivity when the intervalley scattering strength α_{14} is slightly increased. The plot indicates a region in the $B_5 - t_z$ space where the conductivity change is unusual—increasing the intervalley scattering leads to an increase in the conductivity's magnitude. This behavior is consistent even when α_{14} is held constant and α_{12} is varied, hence it is not shown separately. These findings underscore the nuanced interactions between strain-induced fields, scattering strengths, and the tilting of Weyl cones, which collectively influence the planar Hall effect in inversion asymmetric Weyl semimetals.

IV. OUTLOOK

The problem of electron flow in materials has always garnered the attention of physicists. Despite the complex nature of the underlying many-body quantum system, the Boltzmann theory reasonably captures the essential physics in metallic systems, especially when effects originating from quantum interference and entanglement are unimportant. This remains true as long as Bloch's theorem remains a valid assumption in the system. Matter, which was classified by Landau's paradigm of broken symmetry has now evolved into topological matter, where fundamental ideas from topology and geometry have allowed us to study physical systems from a new lens. It is remarkable that these ideas of quan-

tum geometry and topology can be incorporated in the Bloch-Boltzmann formalism [13], and add a whole new dimension to the problem of electron transport in metals. It is important to point out that although a quantum linear-response formalism, such as the one developed by Kubo [160] predicts the behavior in any system, the Boltzmann approach provides an intuitive and physically transparent picture. The study of electron transport in WSMs has explored the full potential of the topological Bloch-Boltzmann formalism, revealing surprising effects such as the chiral magnetic effect and chiral anomaly that were traditionally associated with high-energy physics. The reappearance of the same mathematical structures across different energy and length scales is an astounding feature uncovered in the Bloch-Boltzmann study of WSMs.

Initially, Weyl semimetals were predicted to only display negative longitudinal magnetoresistivity, which was considered to be a smoking gun signature of ‘chiral anomaly’. Several recent works have revisited this problem discovering that magnetoresistivity in LMC is more intricate, and crucially depends on the strength of in-

ternode scattering, the tilt of Weyl nodes, and also the presence of strain. Furthermore, it has been realized that anomalous Hall resistivity, planar Hall magnetoresistivity, Nernst, and thermoelectric conductivities can also provide signatures that reveal the underlying topology and chirality of the Bloch bands, making them striking phenomena of the manifestation of the quantum-mechanical nature of the Weyl wavefunction in macroscopic properties. Several experimental works report nuanced behavior of magnetoresistivity in WSMs that is also fully consistent with the theoretical predictions reviewed in this work [161–163]. In this review, we comprehensively discussed magnetotransport in WSMs, carefully examining the effects of different scattering mechanisms and strain. Although the results presented are valid for a prototype model of only two nodes (or four nodes in case of inversion asymmetric WSMs), the physics is expected to hold for generic Weyl and Dirac systems. We end by stating that the development of toy models into comprehensive theories of real materials and their practical realizations remains a major challenge in contemporary condensed matter physics.

-
- [1] K. v. Klitzing, G. Dorda, and M. Pepper, New method for high-accuracy determination of the fine-structure constant based on quantized hall resistance, *Physical review letters* **45**, 494 (1980).
 - [2] D. C. Tsui, H. L. Stormer, and A. C. Gossard, Two-dimensional magnetotransport in the extreme quantum limit, *Physical Review Letters* **48**, 1559 (1982).
 - [3] R. B. Laughlin, Quantized hall conductivity in two dimensions, *Physical Review B* **23**, 5632 (1981).
 - [4] D. J. Thouless, M. Kohmoto, M. P. Nightingale, and M. den Nijs, Quantized hall conductance in a two-dimensional periodic potential, *Physical review letters* **49**, 405 (1982).
 - [5] R. B. Laughlin, Anomalous quantum hall effect: an incompressible quantum fluid with fractionally charged excitations, *Physical Review Letters* **50**, 1395 (1983).
 - [6] X.-G. Wen, Topological orders and edge excitations in fractional quantum hall states, *Advances in Physics* **44**, 405 (1995).
 - [7] M. V. Berry, Quantal phase factors accompanying adiabatic changes, *Proceedings of the Royal Society of London. A. Mathematical and Physical Sciences* **392**, 45 (1984).
 - [8] M. Z. Hasan and C. L. Kane, Colloquium: topological insulators, *Reviews of modern physics* **82**, 3045 (2010).
 - [9] X.-L. Qi and S.-C. Zhang, Topological insulators and superconductors, *Reviews of modern physics* **83**, 1057 (2011).
 - [10] A. C. Neto, F. Guinea, N. M. Peres, K. S. Novoselov, and A. K. Geim, The electronic properties of graphene, *Reviews of modern physics* **81**, 109 (2009).
 - [11] S. D. Sarma, S. Adam, E. Hwang, and E. Rossi, Electronic transport in two-dimensional graphene, *Reviews of modern physics* **83**, 407 (2011).
 - [12] F. D. M. Haldane, Nobel lecture: Topological quantum matter, *Reviews of Modern Physics* **89**, 040502 (2017).
 - [13] D. Xiao, M.-C. Chang, and Q. Niu, Berry phase effects on electronic properties, *Reviews of modern physics* **82**, 1959 (2010).
 - [14] X.-G. Wen, Colloquium: Zoo of quantum-topological phases of matter, *Reviews of Modern Physics* **89**, 041004 (2017).
 - [15] G. E. Volovik, *The universe in a helium droplet*, Vol. 117 (Oxford University Press on Demand, 2003).
 - [16] P. A. M. Dirac, The quantum theory of the electron, *Proceedings of the Royal Society of London. Series A, Containing Papers of a Mathematical and Physical Character* **117**, 610 (1928).
 - [17] H. Weyl, Gravitation and the electron, *Proceedings of the National Academy of Sciences* **15**, 323 (1929).
 - [18] P. Hosur and X. Qi, Recent developments in transport phenomena in weyl semimetals, *Comptes Rendus. Physique* **14**, 857 (2013).
 - [19] N. Armitage, E. Mele, and A. Vishwanath, Weyl and dirac semimetals in three-dimensional solids, *Reviews of Modern Physics* **90**, 015001 (2018).
 - [20] S. Murakami, Phase transition between the quantum spin hall and insulator phases in 3d: emergence of a topological gapless phase, *New Journal of Physics* **9**, 356 (2007).
 - [21] S. Murakami, S. Iso, Y. Avishai, M. Onoda, and N. Nagaosa, Tuning phase transition between quantum spin hall and ordinary insulating phases, *Physical Review B* **76**, 205304 (2007).
 - [22] G. Xu, H. Weng, Z. Wang, X. Dai, and Z. Fang, Chern semimetal and the quantized anomalous hall effect in hgc2 se4, *Physical Review Letters* **107**, 186806 (2011).
 - [23] X. Wan, A. M. Turner, A. Vishwanath, and S. Y. Savrasov, Topological semimetal and fermi-arc surface states in the electronic structure of pyrochlore iridates,

- Physical Review B **83**, 205101 (2011).
- [24] A. Burkov, M. Hook, and L. Balents, Topological nodal semimetals, Physical Review B **84**, 235126 (2011).
 - [25] A. Burkov and L. Balents, Weyl semimetal in a topological insulator multilayer, Physical Review Letters **107**, 127205 (2011).
 - [26] S.-Y. Xu, N. Alidoust, I. Belopolski, Z. Yuan, G. Bian, T.-R. Chang, H. Zheng, V. N. Strocov, D. S. Sanchez, G. Chang, *et al.*, Discovery of a weyl fermion state with fermi arcs in niobium arsenide, Nature Physics **11**, 748 (2015).
 - [27] N. Xu, H. Weng, B. Lv, C. E. Matt, J. Park, F. Bisti, V. N. Strocov, D. Gawryluk, E. Pomjakushina, K. Conder, *et al.*, Observation of weyl nodes and fermi arcs in tantalum phosphide, Nature communications **7**, 11006 (2016).
 - [28] C. Shekhar, A. K. Nayak, Y. Sun, M. Schmidt, M. Nicklas, I. Leermakers, U. Zeitler, Y. Skourski, J. Wosnitza, Z. Liu, *et al.*, Extremely large magnetoresistance and ultrahigh mobility in the topological weyl semimetal candidate nbp, Nature Physics **11**, 645 (2015).
 - [29] A. A. Soluyanov, D. Gresch, Z. Wang, Q. Wu, M. Troyer, X. Dai, and B. A. Bernevig, Type-ii weyl semimetals, Nature **527**, 495 (2015).
 - [30] B. Lv, N. Xu, H. Weng, J. Ma, P. Richard, X. Huang, L. Zhao, G. Chen, C. Matt, F. Bisti, *et al.*, Observation of weyl nodes in taas, Nature Physics **11**, 724 (2015).
 - [31] L. Yang, Z. Liu, Y. Sun, H. Peng, H. Yang, T. Zhang, B. Zhou, Y. Zhang, Y. Guo, M. Rahn, *et al.*, Weyl semimetal phase in the non-centrosymmetric compound taas, Nature physics **11**, 728 (2015).
 - [32] S.-B. Zhang, H.-Z. Lu, and S.-Q. Shen, Linear magnetoconductivity in an intrinsic topological weyl semimetal, New Journal of Physics **18**, 053039 (2016).
 - [33] H. Weng, C. Fang, Z. Fang, B. A. Bernevig, and X. Dai, Weyl semimetal phase in noncentrosymmetric transition-metal monophosphides, Physical Review X **5**, 011029 (2015).
 - [34] F. Arnold, M. Naumann, S.-C. Wu, Y. Sun, M. Schmidt, H. Borrmann, C. Felser, B. Yan, and E. Hassinger, Chiral weyl pockets and fermi surface topology of the weyl semimetal taas, Physical review letters **117**, 146401 (2016).
 - [35] J. Klotz, S.-C. Wu, C. Shekhar, Y. Sun, M. Schmidt, M. Nicklas, M. Baenitz, M. Uhlarz, J. Wosnitza, C. Felser, *et al.*, Quantum oscillations and the fermi surface topology of the weyl semimetal nbp, Physical Review B **93**, 121105 (2016).
 - [36] T. Liang, Q. Gibson, M. N. Ali, M. Liu, R. J. Cava, and N. P. Ong, Ultrahigh mobility and giant magnetoresistance in the dirac semimetal cd 3 as 2, Nature materials **14**, 280 (2015).
 - [37] S.-M. Huang, S.-Y. Xu, I. Belopolski, C.-C. Lee, G. Chang, B. Wang, N. Alidoust, G. Bian, M. Neupane, C. Zhang, *et al.*, A weyl fermion semimetal with surface fermi arcs in the transition metal monopnictide taas class, Nature communications **6**, 7373 (2015).
 - [38] S.-Y. Xu, I. Belopolski, D. S. Sanchez, M. Neupane, G. Chang, K. Yaji, Z. Yuan, C. Zhang, K. Kuroda, G. Bian, *et al.*, Spin polarization and texture of the fermi arcs in the weyl fermion semimetal taas, Physical review letters **116**, 096801 (2016).
 - [39] M. Z. Hasan, G. Chang, I. Belopolski, G. Bian, S.-Y. Xu, and J.-X. Yin, Weyl, dirac and high-fold chiral fermions in topological quantum matter, Nature Reviews Materials **6**, 784 (2021).
 - [40] S. L. Adler, Axial-vector vertex in spinor electrodynamics, Physical Review **177**, 2426 (1969).
 - [41] J. S. Bell and R. Jackiw, A pcac puzzle: $\pi \rightarrow \gamma\gamma$ in the σ -model, Il Nuovo Cimento A (1965-1970) **60**, 47 (1969).
 - [42] H. B. Nielsen and M. Ninomiya, *No-go theorem for regularizing chiral fermions*, Tech. Rep. (Science Research Council, 1981).
 - [43] H. B. Nielsen and M. Ninomiya, The adler-bell-jackiw anomaly and weyl fermions in a crystal, Physics Letters B **130**, 389 (1983).
 - [44] A. Zyuzin, S. Wu, and A. Burkov, Weyl semimetal with broken time reversal and inversion symmetries, Physical Review B **85**, 165110 (2012).
 - [45] D. Son and B. Spivak, Chiral anomaly and classical negative magnetoresistance of weyl metals, Physical Review B **88**, 104412 (2013).
 - [46] P. Goswami and S. Tewari, Axionic field theory of (3+1)-dimensional weyl semimetals, Physical Review B **88**, 245107 (2013).
 - [47] P. Goswami, J. Pixley, and S. D. Sarma, Axial anomaly and longitudinal magnetoresistance of a generic three-dimensional metal, Physical Review B **92**, 075205 (2015).
 - [48] S. Zhong, J. Orenstein, and J. E. Moore, Optical gyrotropy from axion electrodynamics in momentum space, Physical Review Letters **115**, 117403 (2015).
 - [49] K.-S. Kim, H.-J. Kim, and M. Sasaki, Boltzmann equation approach to anomalous transport in a weyl metal, Physical Review B **89**, 195137 (2014).
 - [50] R. Lundgren, P. Laurell, and G. A. Fiete, Thermoelectric properties of weyl and dirac semimetals, Physical Review B **90**, 165115 (2014).
 - [51] A. Cortijo, Linear magnetochiral effect in weyl semimetals, Physical Review B **94**, 241105 (2016).
 - [52] G. Sharma, P. Goswami, and S. Tewari, Nernst and magnetothermal conductivity in a lattice model of weyl fermions, Physical Review B **93**, 035116 (2016).
 - [53] V. A. Zyuzin, Magnetotransport of weyl semimetals due to the chiral anomaly, Physical Review B **95**, 245128 (2017).
 - [54] K. Das and A. Agarwal, Berry curvature induced thermopower in type-i and type-ii weyl semimetals, Physical Review B **100**, 085406 (2019).
 - [55] A. Kundu, Z. B. Siu, H. Yang, and M. B. Jalil, Magnetotransport of weyl semimetals with tilted dirac cones, New Journal of Physics **22**, 083081 (2020).
 - [56] A. Knoll, C. Timm, and T. Meng, Negative longitudinal magnetoconductance at weak fields in weyl semimetals, Physical Review B **101**, 201402 (2020).
 - [57] G. Sharma, S. Nandy, and S. Tewari, Sign of longitudinal magnetoconductivity and the planar hall effect in weyl semimetals, Physical Review B **102**, 205107 (2020).
 - [58] G. Bednik, K. Tikhonov, and S. Syzranov, Magnetotransport and internodal tunnelling in weyl semimetals, Physical Review Research **2**, 023124 (2020).
 - [59] L. He, X. Hong, J. Dong, J. Pan, Z. Zhang, J. Zhang, and S. Li, Quantum transport evidence for the three-dimensional dirac semimetal phase in cd 3 as 2, Physical Review Letters **113**, 246402 (2014).
 - [60] C.-L. Zhang, S.-Y. Xu, I. Belopolski, Z. Yuan, Z. Lin,

- B. Tong, G. Bian, N. Alidoust, C.-C. Lee, S.-M. Huang, *et al.*, Signatures of the adler–bell–jackiw chiral anomaly in a weyl fermion semimetal, *Nature communications* **7**, 1 (2016).
- [61] Q. Li, D. E. Kharzeev, C. Zhang, Y. Huang, I. Pletikosić, A. Fedorov, R. Zhong, J. Schneeloch, G. Gu, and T. Valla, Chiral magnetic effect in ZrTe_5 , *Nature Physics* **12**, 550 (2016).
- [62] J. Xiong, S. K. Kushwaha, T. Liang, J. W. Krizan, M. Hirschberger, W. Wang, R. J. Cava, and N. P. Ong, Evidence for the chiral anomaly in the dirac semimetal Na_3Bi , *Science* **350**, 413 (2015).
- [63] M. Hirschberger, S. Kushwaha, Z. Wang, Q. Gibson, S. Liang, C. A. Belvin, B. A. Bernevig, R. J. Cava, and N. P. Ong, The chiral anomaly and thermopower of weyl fermions in the half-Heusler GdPtBi , *Nature materials* **15**, 1161 (2016).
- [64] S. Nandy, G. Sharma, A. Taraphder, and S. Tewari, Chiral anomaly as the origin of the planar hall effect in weyl semimetals, *Physical Review Letters* **119**, 176804 (2017).
- [65] K. Das and A. Agarwal, Linear magnetochiral transport in tilted type-i and type-ii weyl semimetals, *Physical Review B* **99**, 085405 (2019).
- [66] G. Sharma and S. Tewari, Transverse thermopower in dirac and weyl semimetals, *Physical Review B* **100**, 195113 (2019).
- [67] G. Sharma, S. Nandy, K. V. Raman, and S. Tewari, Decoupling intranode and internode scattering in weyl fermions, *Physical Review B* **107**, 115161 (2023).
- [68] A. Ahmad and G. Sharma, Longitudinal magnetoconductance and the planar hall effect in a lattice model of tilted weyl fermions, *Physical Review B* **103**, 115146 (2021).
- [69] A. Ahmad, K. V. Raman, S. Tewari, and G. Sharma, Longitudinal magnetoconductance and the planar hall conductance in inhomogeneous weyl semimetals, *Physical Review B* **107**, 144206 (2023).
- [70] G. Varma, A. Ahmad, S. Tewari, and G. Sharma, Magnetotransport in spin-orbit coupled noncentrosymmetric and weyl metals, *Physical Review B* **109**, 165114 (2024).
- [71] G. Sharma, P. Goswami, and S. Tewari, Chiral anomaly and longitudinal magnetotransport in type-ii weyl semimetals, *Physical Review B* **96**, 045112 (2017).
- [72] G. Sharma, C. Moore, S. Saha, and S. Tewari, Nernst effect in dirac and inversion-asymmetric weyl semimetals, *Physical Review B* **96**, 195119 (2017).
- [73] P. Goswami, G. Sharma, and S. Tewari, Optical activity as a test for dynamic chiral magnetic effect of weyl semimetals, *Physical Review B* **92**, 161110 (2015).
- [74] A. L. Levy, A. B. Sushkov, F. Liu, B. Shen, N. Ni, H. D. Drew, and G. S. Jenkins, Optical evidence of the chiral magnetic anomaly in the weyl semimetal TaAs , *Physical Review B* **101**, 125102 (2020).
- [75] J.-M. Parent, R. Côté, and I. Garate, Magneto-optical kerr effect and signature of the chiral anomaly in a weyl semimetal in magnetic field, *Physical Review B* **102**, 245126 (2020).
- [76] Z. Song, J. Zhao, Z. Fang, and X. Dai, Detecting the chiral magnetic effect by lattice dynamics in weyl semimetals, *Physical Review B* **94**, 214306 (2016).
- [77] P. Rinkel, P. L. Lopes, and I. Garate, Signatures of the chiral anomaly in phonon dynamics, *Physical Review Letters* **119**, 107401 (2017).
- [78] X. Yuan, C. Zhang, Y. Zhang, Z. Yan, T. Lyu, M. Zhang, Z. Li, C. Song, M. Zhao, P. Leng, *et al.*, The discovery of dynamic chiral anomaly in a weyl semimetal NbAs , *Nature communications* **11**, 1 (2020).
- [79] B. Cheng, T. Schumann, S. Stemmer, and N. Armitage, Probing charge pumping and relaxation of the chiral anomaly in a dirac semimetal, *arXiv preprint arXiv:1910.13655* (2019).
- [80] A. G. Grushin, J. W. Venderbos, A. Vishwanath, and R. Ilan, Inhomogeneous weyl and dirac semimetals: Transport in axial magnetic fields and fermi arc surface states from pseudo-landau levels, *Physical Review X* **6**, 041046 (2016).
- [81] T. Needham, *Visual differential geometry and forms: a mathematical drama in five acts* (Princeton University Press, 2021).
- [82] M. Nakahara, *Geometry, topology and physics* (CRC press, 2018).
- [83] P. A. M. Dirac, Quantised singularities in the electromagnetic field, *Proceedings of the Royal Society of London. Series A, Containing Papers of a Mathematical and Physical Character* **133**, 60 (1931).
- [84] T. T. Wu and C. N. Yang, Concept of nonintegrable phase factors and global formulation of gauge fields, *Physical Review D* **12**, 3845 (1975).
- [85] M. E. Peskin, *An introduction to quantum field theory* (CRC press, 2018).
- [86] C. Herring, Accidental degeneracy in the energy bands of crystals, *Physical Review* **52**, 365 (1937).
- [87] J. Smit, *Introduction to quantum fields on a lattice* (Cambridge University Press, 2003).
- [88] D. Friedan, A proof of the nielsen-ninomiya theorem, *Communications in Mathematical Physics* **85**, 481 (1982).
- [89] A. Burkov, Anomalous hall effect in weyl metals, *Physical Review Letters* **113**, 187202 (2014).
- [90] S. Parameswaran, T. Grover, D. Abanin, D. Pesin, and A. Vishwanath, Probing the chiral anomaly with nonlocal transport in three-dimensional topological semimetals, *Physical Review X* **4**, 031035 (2014).
- [91] M. Imran and S. Hershfield, Berry curvature force and lorentz force comparison in the magnetotransport of weyl semimetals, *Physical Review B* **98**, 205139 (2018).
- [92] N. W. Ashcroft, *Nd mermin solid state physics*, Saunders College, Philadelphia **120** (1976).
- [93] D. T. Son and N. Yamamoto, Berry curvature, triangle anomalies, and the chiral magnetic effect in fermi liquids, *Physical Review Letters* **109**, 181602 (2012).
- [94] H. Bruus and K. Flensberg, *Many-body quantum theory in condensed matter physics: an introduction* (Oxford university press, 2004).
- [95] G. D. Mahan, *9. Many-Particle Systems* (Princeton University Press, 2008).
- [96] K. Fukushima, D. E. Kharzeev, and H. J. Warringa, Chiral magnetic effect, *Physical Review D* **78**, 074033 (2008).
- [97] R. Dos Reis, M. Ajeesh, N. Kumar, F. Arnold, C. Shekhar, M. Naumann, M. Schmidt, M. Nicklas, and E. Hassinger, On the search for the chiral anomaly in weyl semimetals: The negative longitudinal magnetoresistance, *New Journal of Physics* **18**, 085006 (2016).
- [98] M.-M. Wu, Y. Sun, J. Li, H. Zhao, and H. Pan, Valley-dependent electron scattering in weyl semimetals, *Solid*

- State Communications **334**, 114387 (2021).
- [99] A. Lucas, R. A. Davison, and S. Sachdev, Hydrodynamic theory of thermoelectric transport and negative magnetoresistance in weyl semimetals, *Proceedings of the National Academy of Sciences* **113**, 9463 (2016).
 - [100] B. Spivak and A. Andreev, Magnetotransport phenomena related to the chiral anomaly in weyl semimetals, *Physical Review B* **93**, 085107 (2016).
 - [101] A. Burkov, Chiral anomaly and diffusive magnetotransport in weyl metals, *Physical review letters* **113**, 247203 (2014).
 - [102] K. Kim, H. C. Choi, and B. Min, Fermi surface and surface electronic structure of delafossite PdCoO_2 , *Physical Review B* **80**, 035116 (2009).
 - [103] H.-J. Noh, J. Jeong, J. Jeong, E.-J. Cho, S. B. Kim, K. Kim, B. Min, and H.-D. Kim, Anisotropic electric conductivity of delafossite PdCoO_2 studied by angle-resolved photoemission spectroscopy, *Physical Review Letters* **102**, 256404 (2009).
 - [104] N. Kikugawa, P. Goswami, A. Kiswandhi, E. Choi, D. Graf, R. Baumbach, J. Brooks, K. Sugii, Y. Iida, M. Nishio, *et al.*, Interplanar coupling-dependent magnetoresistivity in high-purity layered metals, *Nature communications* **7**, 1 (2016).
 - [105] S. Liang, J. Lin, S. Kushwaha, J. Xing, N. Ni, R. J. Cava, and N. P. Ong, Experimental tests of the chiral anomaly magnetoresistance in the dirac-weyl semimetals Na_3Bi and GdPtBi , *Physical Review X* **8**, 031002 (2018).
 - [106] H.-Z. Lu, S.-B. Zhang, and S.-Q. Shen, High-field magnetoconductivity of topological semimetals with short-range potential, *Physical Review B* **92**, 045203 (2015).
 - [107] C.-Z. Chen, H. Liu, H. Jiang, and X. Xie, Positive magnetoconductivity of weyl semimetals in the ultraquantum limit, *Physical Review B* **93**, 165420 (2016).
 - [108] J. Shao and L. Yan, Magneto-conductivity of tilted type-i weyl semimetals with different types of impurities, *AIP Advances* **9**, 045319 (2019).
 - [109] X. Li, B. Roy, and S. D. Sarma, Weyl fermions with arbitrary monopoles in magnetic fields: Landau levels, longitudinal magnetotransport, and density-wave ordering, *Physical Review B* **94**, 195144 (2016).
 - [110] X.-T. Ji, H.-Z. Lu, Z.-G. Zhu, and G. Su, Effect of the screened coulomb disorder on magneto-transport in weyl semimetals, *Journal of Applied Physics* **123**, 203901 (2018).
 - [111] R. M. Dantas, F. Peña-Benitez, B. Roy, and P. Surówka, Magnetotransport in multi-weyl semimetals: A kinetic theory approach, *Journal of High Energy Physics* **2018**, 69 (2018).
 - [112] A. Johansson, J. Henk, and I. Mertig, Chiral anomaly in type-i weyl semimetals: Comprehensive analysis within a semiclassical fermi surface harmonics approach, *Physical Review B* **99**, 075114 (2019).
 - [113] R. Jackiw and S.-Y. Pi, Chiral gauge theory for graphene, *Physical review letters* **98**, 266402 (2007).
 - [114] M. A. Vozmediano, M. Katsnelson, and F. Guinea, Gauge fields in graphene, *Physics Reports* **496**, 109 (2010).
 - [115] F. Guinea, M. Katsnelson, and A. Geim, Energy gaps and a zero-field quantum hall effect in graphene by strain engineering, *Nature Physics* **6**, 30 (2010).
 - [116] A. Cortijo, Y. Ferreirós, K. Landsteiner, and M. A. Vozmediano, Elastic gauge fields in weyl semimetals, *Physical Review Letters* **115**, 177202 (2015).
 - [117] D. Pikulin, A. Chen, and M. Franz, Chiral anomaly from strain-induced gauge fields in dirac and weyl semimetals, *Physical Review X* **6**, 041021 (2016).
 - [118] N. Levy, S. Burke, K. Meaker, M. Panlasigui, A. Zettl, F. Guinea, A. C. Neto, and M. F. Crommie, Strain-induced pseudo-magnetic fields greater than 300 tesla in graphene nanobubbles, *Science* **329**, 544 (2010).
 - [119] E. T. Sisakht, F. Fazileh, M. Zare, M. Zarenia, and F. Peeters, Strain-induced topological phase transition in phosphorene and in phosphorene nanoribbons, *Physical Review B* **94**, 085417 (2016).
 - [120] C. Niu, Z. Zhang, D. Graf, S. Lee, M. Wang, W. Wu, T. Low, and P. D. Ye, High-pressure induced weyl semimetal phase in 2d tellurium, *Communications Physics* **6**, 345 (2023).
 - [121] L. Thulin and J. Guerra, Calculations of strain-modified anatase TiO_2 band structures, *Physical Review B* **77**, 195112 (2008).
 - [122] K.-H. Hong, J. Kim, S.-H. Lee, and J. K. Shin, Strain-driven electronic band structure modulation of Si nanowires, *Nano letters* **8**, 1335 (2008).
 - [123] Q. Yan, P. Rinke, A. Janotti, M. Scheffler, and C. G. Van de Walle, Effects of strain on the band structure of group-iii nitrides, *Physical Review B* **90**, 125118 (2014).
 - [124] G. Gui, J. Li, and J. Zhong, Band structure engineering of graphene by strain: First-principles calculations, *Physical Review B* **78**, 075435 (2008).
 - [125] Y. Miao, Y. Zhao, S. Zhang, R. Shi, and T. Zhang, Strain engineering: a boosting strategy for photocatalysis, *Advanced Materials* **34**, 2200868 (2022).
 - [126] H. Rostami, R. Roldán, E. Cappelluti, R. Asgari, and F. Guinea, Theory of strain in single-layer transition metal dichalcogenides, *Physical Review B* **92**, 195402 (2015).
 - [127] H. Peelaers and C. G. Van de Walle, Effects of strain on band structure and effective masses in MoS_2 , *Physical Review B* **86**, 241401 (2012).
 - [128] B. Lazarovits, K. Kim, K. Haule, and G. Kotliar, Effects of strain on the electronic structure of VO_2 , *Physical Review B* **81**, 115117 (2010).
 - [129] A. Janotti, D. Steiauf, and C. Van de Walle, Strain effects on the electronic structure of SrTiO_3 : Toward high electron mobilities, *Physical Review B* **84**, 201304 (2011).
 - [130] J. Hwang, C. K. Shih, P. Pianetta, G. Kubiak, R. Stulen, L. Dawson, Y.-C. Pao, and J. Harris Jr, Effect of strain on the band structure of GaAs and $\text{In}_0.2\text{Ga}_{0.8}\text{As}$, *Applied physics letters* **52**, 308 (1988).
 - [131] K. Sakata, B. Magyari-Köpe, S. Gupta, Y. Nishi, A. Blom, and P. Deák, The effects of uniaxial and biaxial strain on the electronic structure of germanium, *Computational Materials Science* **112**, 263 (2016).
 - [132] D. Sabsovich, T. Meng, D. I. Pikulin, R. Queiroz, and R. Ilan, Pseudo field effects in type ii weyl semimetals: new probes for over tilted cones, *Journal of Physics: Condensed Matter* **32**, 484002 (2020).
 - [133] N. Christensen, Electronic structure of GaAs under strain, *Physical Review B* **30**, 5753 (1984).
 - [134] P. V. Arribi, J.-X. Zhu, T. Schumann, S. Stemmer, A. A. Burkov, and O. Heinonen, Topological surface states in strained dirac semimetal thin films, *Physical Review B* **102**, 155141 (2020).
 - [135] Q.-D. Jiang, H. Jiang, H. Liu, Q.-F. Sun, and X.-C.

- Xie, Topological imbert-fedorov shift in weyl semimetals, *Physical review letters* **115**, 156602 (2015).
- [136] R. Ghosh and I. Mandal, Electric and thermoelectric response for weyl and multi-weyl semimetals in planar hall configurations including the effects of strain, *Physica E: Low-dimensional Systems and Nanostructures* **159**, 115914 (2024).
 - [137] S. Heidari and R. Asgari, Chiral hall effect in strained weyl semimetals, *Physical Review B* **101**, 165309 (2020).
 - [138] S. A. Yang, H. Pan, and F. Zhang, Chirality-dependent hall effect in weyl semimetals, *Physical review letters* **115**, 156603 (2015).
 - [139] G. Volovik, On induced cpt-odd chern-simons terms in the 3+ 1 effective action, *Journal of Experimental and Theoretical Physics Letters* **70**, 1 (1999).
 - [140] C.-X. Liu, P. Ye, and X.-L. Qi, Chiral gauge field and axial anomaly in a weyl semimetal, *Physical Review B* **87**, 235306 (2013).
 - [141] A. G. Grushin, Consequences of a condensed matter realization of lorentz-violating qed in weyl semi-metals, *Physical Review D* **86**, 045001 (2012).
 - [142] A. Zyuzin and A. Burkov, Topological response in weyl semimetals and the chiral anomaly, *Physical Review B* **86**, 115133 (2012).
 - [143] S. Ghosh, D. Sinha, S. Nandy, and A. Taraphder, Chirality-dependent planar hall effect in inhomogeneous weyl semimetals, *Physical Review B* **102**, 121105 (2020).
 - [144] A. Burkov, Chiral anomaly and nonlocal transport in weyl semimetals, *Physical Review B* **96**, 041110 (2017).
 - [145] V. D. Ky, Effect of deformation on the thermoelectric power of indium antimonide, *Phys. Status Solidi* **26**, 565 (1968).
 - [146] Z. Ge, W. Lim, S. Shen, Y. Zhou, X. Liu, J. Furdyna, and M. Dobrowolska, Magnetization reversal in (ga, mn) as/mno exchange-biased structures: Investigation by planar hall effect, *Physical Review B* **75**, 014407 (2007).
 - [147] K. Friedland, M. Bowen, J. Herfort, H. Schönherr, and K. Ploog, High curie temperature and anisotropy in gamnas/gaalas/gamnas trilayers, *Journal of Physics: Condensed Matter* **18**, 2641 (2006).
 - [148] S. Goennenwein, R. Keizer, S. Schink, I. van Dijk, T. Klapwijk, G. Miao, G. Xiao, and A. Gupta, Spin injection and detection in all-metallic planar spin valves with cu, al, and ag spacers, *Applied Physics Letters* **90**, 142509 (2007).
 - [149] M. Bowen, K. Friedland, J. Herfort, H. Schönherr, and K. Ploog, Large inverse tunneling magnetoresistance in cofe/alox/cofe magnetic tunnel junctions with mgo (100) barriers, *Physical Review B* **71**, 172401 (2005).
 - [150] D. Ma, H. Jiang, H. Liu, and X. Xie, Planar hall effect in tilted weyl semimetals, *Physical Review B* **99**, 115121 (2019).
 - [151] L. Medel Onofre and A. Martín-Ruiz, Planar hall effect in weyl semimetals induced by pseudoelectromagnetic fields, *Physical Review B* **108**, 155132 (2023).
 - [152] S. Das, K. Das, and A. Agarwal, Chiral anomalies in three-dimensional spin-orbit coupled metals: Electrical, thermal, and gravitational anomalies, *Physical Review B* **108**, 045405 (2023).
 - [153] N. Kumar, S. N. Guin, C. Felser, and C. Shekhar, Planar hall effect in the weyl semimetal gdptbi, *Physical Review B* **98**, 041103 (2018).
 - [154] J. Yang, W. Zhen, D. Liang, Y. Wang, X. Yan, S. Weng, J. Wang, W. Tong, L. Pi, W. Zhu, *et al.*, Current jetting distorted planar hall effect in a weyl semimetal with ultrahigh mobility, *Physical Review Materials* **3**, 014201 (2019).
 - [155] H. Li, H.-W. Wang, H. He, J. Wang, and S.-Q. Shen, Giant anisotropic magnetoresistance and planar hall effect in the dirac semimetal cd 3 as 2, *Physical Review B* **97**, 201110 (2018).
 - [156] F. Chen, X. Luo, J. Yan, Y. Sun, H. Lv, W. Lu, C. Xi, P. Tong, Z. Sheng, X. Zhu, *et al.*, Planar hall effect in the type-ii weyl semimetal t d- mot e 2, *Physical Review B* **98**, 041114 (2018).
 - [157] P. Li, C. Zhang, J. Zhang, Y. Wen, and X. Zhang, Giant planar hall effect in the dirac semimetal zrt e 5- δ , *Physical Review B* **98**, 121108 (2018).
 - [158] O. Pavlosiuk, D. Kaczorowski, and P. Wiśniewski, Negative longitudinal magnetoresistance as a sign of a possible chiral magnetic anomaly in the half-heusler antiferromagnet dypdbi, *Physical Review B* **99**, 125142 (2019).
 - [159] R. Singha, S. Roy, A. Pariari, B. Satpati, and P. Mandal, Planar hall effect in the type-ii dirac semimetal val 3, *Physical Review B* **98**, 081103 (2018).
 - [160] R. Kubo, Statistical-mechanical theory of irreversible processes. i. general theory and simple applications to magnetic and conduction problems, *Journal of the physical society of Japan* **12**, 570 (1957).
 - [161] A. Flessa Savvidou, A. Ptok, G. Sharma, B. Casas, J. K. Clark, V. M. Li, M. Shatruk, S. Tewari, and L. Balicas, Anisotropic positive linear and sub-linear magnetoresistivity in the cubic type-ii dirac metal pd3in7, *npj Quantum Materials* **8**, 68 (2023).
 - [162] Sonika, S. Gangwar, N. S. Mehta, G. Sharma, and C. Yadav, Chiral anomaly and positive longitudinal magnetoresistance in the type-ii dirac semimetals a x pdte 2 (a= cu, ag), *Physical Review B* **108**, 245141 (2023).
 - [163] A. N. Tamanna, A. Lakra, X. Ding, E. Buzi, K. Park, K. Sobczak, H. Deng, G. Sharma, S. Tewari, and L. Krusin-Elbaum, Hydrogen induces chiral conduction channels in the topological magnet, *arXiv preprint arXiv:2312.02315* (2023).